The effects of inductive electric field on the spatial and temporal evolution of inner magnetospheric ring current

Jianghuai Liu[1], **Raluca Ilie**[1]

[1]University of Illinois, Department of Electrical and Computer Engineering

Key Points:

- Important theoretical and numerical improvements to the HEIDI model have been made in order to incorporate 3 inductive electric field models, and the effect on the ring current ions' total drift, energization rate and pitch-angle change are tested for the first time.
- The inductive electric field acts as an effective local accelerator and provides notable energization rate independent with ions' energy.
- The rapidly changing magnetic field produces large inductive electric field that can dominate over the electrostatic field, thus the inductive electric field can play an important role in shaping ring current topology and energizing ring current hot ion species during storm time.

Corresponding author: Jianghuai Liu, jliu115@illinois.edu

Abstract

Charged particles are observed to be injected into the inner magnetosphere region from plasma sheet, and energized up to high energies over short distance and time, during both geomagnetic storms and substorms. Numerous studies suggest that it is the short-duration and high-speed plasma flows, which are closely associated with the global effects of magnetic reconnection and inductive effects, rather than the slow and steady convection that control the Earth-ward plasma transport and magnetic flux from the magnetotail, especially during geomagnetic activities. In order to include the effect of inductive electric produced by the temporal change of magnetic field on the dynamics of ring current, we implemented both theoretical and numerical modifications to an inner magnetosphere kinetic model—Hot Electron-Ion Drift Integrator (HEIDI). New drift terms associated with the inductive electric field are incorporated into the calculation of bounce-averaged coefficients for the distribution function, and their numerical implementations and the associated effects on total drift and energization rate are discussed. Numerical simulations show that the local particle drifts are significantly altered by the presence of inductive electric fields, in addition to the changing magnetic gradient-curvature drift due to the distortion of magnetic field, and at certain locations, the inductive drift dominates both the potential and the magnetic gradient-curvature drift. The presence of a self-consistent inductive electric field alters the overall particle trajectories, energization, and pitch angle, resulting in significant changes in the topology and strength of the ring current.

1 Introduction

Energetic ions with energies over hundreds of $keVs$ are frequently observed in the near-Earth region during magnetospheric storms and substorms. These hot ions could be transported from the magnetotail into inner magnetosphere through magnetospheric convection, or accelerated locally in the inner magnetosphere. Some of the energy that supports the transport and acceleration of hot ion species within inner magnetosphere is attributed to the energy released during magnetic reconnections, which propagates toward the Earth in the form of electromagnetic disturbances embedded into strong plasma flows (Angelopoulos et al., 1994; Angelopoulos et al., 2013; Zaharia et al., 2005). Dissipation of this energy in the inner magnetosphere provides local ion transport and acceleration. Sudden enhancements of injections of energetic charged particles (tens to hundreds of keV)in the magnetotail are known as Bursty Bulk Flows (BBFs), often asso-

ciated with substorms. These enhancements of injections and energization of charged particles during storms and substorms can be substantial, with particle fluxes measured at the geostationary orbit, increasing by 2 or 3 orders of magnitude as compared to the quiet times (Birn et al., 1997; V. A. Sergeev, Angelopoulos, & Nakamura, 2012; Zaharia, Cheng, & Johnson, 2000). Evidence from satellite observations shows that injections usually originate in the mid-tail region, anywhere between the geostationary orbit and 30 R_E, or even further downstream (Gabrielse, Angelopoulos, Runov, & Turner, 2014). Many of these injections in this relatively distant tail region are clearly associated with BBFs that propagates earthward (Runov et al., 2013). However, a combination of ground-based and satellite observations also discovered that numerous injections start closer in, between 6.6 and 9 R_E in a radially narrow (usually less than 1 R_E) area (Spanswick, Donovan, Friedel, & Korth, 2007; Spanswick, Reeves, Donovan, & Friedel, 2010), which means that energetic charged particles have the potential to penetrate deep into the low L-shell region, causing significant flux enhancement. Such deep penetrations of energetic charged particles events with tens to hundreds of keV electrons and tens of keV protons into the low L-shells ($L < 4$), have been reported by Van Allen Probes measurements, during the storm of April 8, 2016 (Zhao et al., 2017). Furthermore, the ion fluxes with a broad range of energies are sometimes observed to increase dramatically and nearly simultaneously, events known as dispersionless injections, which can be associated with to substorm onset. While much effort has been made to understand these injections during storms and substorms, many details still remain unclear. For example, the dispersionless injections need an explanation based on either a local energization process at the measurement point, or a very rapid transport mechanism. In addition, to describe local acceleration of thermal ions (with energy $\leq 10keV$) to sufficiently high energies ($\geq 100keV$), one needs to propose an effective acceleration mechanism that can be realized in the inner magnetosphere.

As ions and electrons are injected from the plasma sheet to stronger magnetic field regions in the inner magnetosphere, they gain energy consistent with conservation of the first adiabatic invariant, $\mu_m = \frac{W_\perp}{B}$, where $W_\perp = \frac{1}{2}mv_\perp^2$ is the perpendicular kinetic energy of the particle with respect to the magnetic field line, and B is the local magnetic field strength. It is the increase of local magnetic field strength observed by the particle as it drifts toward the Earth that causes the increase of its perpendicular kinetic energy. Dispersionless injections of charged particles from weaker magnetic field regions

to stronger magnetic field regions, in light of its energy-independent energization mechanism, could be driven by the strong electric drift $\mathbf{v} = \mathbf{E} \times \mathbf{B}$ (Ashour-Abdalla et al., 2009; Delcourt, 2002; Gabrielse, Angelopoulos, Runov, & Turner, 2012; Lejosne & Mozer, 2016; Zaharia et al., 2000), which is applied to all particles that constitute a plasma regardless of their mass, energy, and electric charge. In this case, not only the large-scale (extends over several R_E and can lasts for hours) duskward convection electric field, but also the smaller-scale impulsive electric fields, play an important role in the injection and energization of ring current particles, as they also contribute to the $\mathbf{E}\times\mathbf{B}$ flow of plasma into the inner magnetosphere (Ebihara & Ejiri, 1998; Fok, Moore, & Greenspan, 1996; Ganushkina, Liemohn, & Pulkkinen, 2012; Thaller et al., 2015). Storm time enhancements of the large-scale duskward convection electric field has been observed by many spacecraft missions. For instance, Wygant et al. (1998) studied the electric field during the major storm of March 1991 (with minimum Dst around $-300\ nT$) based on measurements from Combined Release and Radiation Effects Satellite (CRRES), and illustrated that the steady duskward component of the large-scale electric field was enhanced from 2 to 6 $\frac{mV}{m}$ near midnight, with a duration ranging from 20 minutes to 5 hours. The enhanced convection electric field facilitated the injection of ions from $L = 8$ down to $L = 2.4$ in about 1 hour, while also energizing them from $15keV$ to $300keV$. Furthermore, such duskward convection electric field plays an important role in ring current enhancement during storm time. Using the Van Allen Probes data, Thaller et al. (2015) found close coincidence between the spatial extent of the enhanced convection electric field and that of the ring current pressure increase and plasmasphere erosion during the June 1, 2013 storm. This confirmed the idea that, observed large-scale convection electric field can transport ions and electrons from the plasma sheet location and energies, to the locations and energies of the ring current particles.

Besides storm time injections, earthward plasma flows from plasmasheet during substorms were also confirmed by Cluster and Time History of Events and Macroscale Interactions during Substorms (THEMIS) observations (Nakamura et al., 2002; V. Sergeev et al., 2009a). Such substorm injections are always associated with dipolarization events, which are characterized by the rapid change of magnetic field from stretched, tail-like to a more dipolar magnetic field. Dipolarization events may involve a brief earthward moving dipolarization pulse, called "dipolarization front", which is observed as a region of rapid increase in the northward magnetic field component, serving as the sharp bound-

ary separating energetic plasma from neighboring plasma sheet (V. Sergeev et al., 2009a, 2009b). THEMIS observations had revealed an interesting property of electric field dynamics associated with the dipolarization front: an intense and short-lived (usually less than 1 minute) dawn-to-dusk electric field pulse has been accompanying the earthward propagating dipolarization front (J. Liu, Angelopoulos, Zhou, & Runov, 2014). This strong electric field pulse has been suggested to be generated from the acceleration of dipolarization front, caused by the imbalance between curvature force and ambient pressure gradients, or the inductive effects due to the slow-down of dipolarization front as it penetrates into strong magnetic field regions of the inner magnetosphere (Artemyev, Liu, Angelopoulos, & Runov, 2015). Unlike large-scale duskward convection electric field, such electric pulses observed during substorms and dipolarization process are small-scale and transient. Using THEMIS data in conjuncture with test particle modeling, Artemyev et al. (2015) has suggested that such pulses can effectively accelerate ions with initial energy of tens of keV up to hundreds of keV. This energization takes place because the ring current ion gyroradius is comparable to the spatial scale of the localized electric field pulse. Consequently, the transient electric pulses observed during substorms serve as an effective local accelerator of charged particles, which possess more inductive nature as it is closely associated with the rapid change of magnetic field during dipolarization.

It is, therefore, important for inner magnetosphere ring current models to incorporate a comprehensive description of the electric field that depends on magnetic activity, since electric field triggers energy-independent $\mathbf{E}\times\mathbf{B}$ drifts that greatly affects the injections of energetic particles into inner magnetosphere, thus has a great impact on the energy profile of ring current population. A typical approach of inner magnetospheric electric field modeling is to first determine the electric potentials Φ, and based on that determine the electrostatic electric field. The analysis and calculation of electric potential Φ can be performed either around the magnetic equator (Matsui, Jordanova, Quinn, Torbert, & Paschmann, 2004; Stern, 1975; Volland, 1973) or in the ionosphere (Richmond et al., 1980), then extend Φ to the entire inner magnetosphere by mapping along each individual equipotential field lines, under the assumption that the potential drop along field line is negligible. This way of treating electric field intrinsically assumes an electrostatic nature of the convection electric field, neglecting the inductive electric field produced by the temporal changes of magnetic field. Such an assumption could be valid, if the required simulation temporal resolution is low, so that we consider the electric field

averaged over a long time interval. This could be the case for low geomagnetic activity, when the geomagnetic field environment is stable, thus the electrostatic component of electric field dominates over the inductive component. However, during magnetic disturbance, small-scale and transient electric field may become the dominant local acceleration mechanism around the midnight sector. Furthermore, it has been shown that a localized temporal change in the magnetic field produces an inductive electric field whose effect extends over all space, meaning that the effect of inductive electric field is global even if the temporal changes in the magnetic field are localized (Ilie, Daldorff, Liemohn, Toth, & Chan, 2017). Treating the electric field only in an electrostatic sense that changes slowly in time and possess large scaling in space, will result in the failure to capture the smaller-scale and transient inductive electric field, leading to an under- or overestimation of energetic particle fluxes and total energy of ring current population.

Despite the underlying importance of inductive electric fields and their contribution to the transport and energization of inner magnetosphere charged particles during magnetic disturbances, modeling the inductive electric field in a self-consistent way is a challenging task, since it requires adequate decomposition strategies depending on the specific storm situations and available information, and the computational cost is usually large in 3-D code (Ilie et al., 2017; Toivanen, 2007; Zaharia, Jordanova, Thomsen, & Reeves, 2008). Some simplistic models for the inductive electric field (Li, Baker, Temerin, Reeves, & Belian, 1998; Sarris, Li, Tsaggas, & Paschalidis, 2002) have been adopted in drift and transport models to explain and investigate these particle injections into inner magnetosphere (Ganushkina, Pulkkinen, Bashkirov, Baker, & Li, 2001). In addition, the effect of the inductive electric field has been included in some models by tracing the displacement of magnetic field lines in the process of magnetic reconfiguration, under the assumption that the ionospheric foot-point of each field line stays fixed (Fok & Moore, 1997), which could be invalidated by the ionospheric foot-point advection. In this paper, we describe recent developments made to a kinetic ring current model, the Hot Electron-Ion Drift Integrator (HEIDI) model, to include the effect of inductive electric field in modeling the drift and energization of interested ring current ion population. We investigated the effect of the inductive field, based on three inductive electric field models within the numerical domain of HEIDI, and analyzed the corresponding changes to the drift and energization rate. First, we imposed a dawn-dusk electric field as the inductive component, whose polarization and magnitude depends on Magnetic Local Time (MLT), across

the entire HEIDI domain, to depict the global topology of such fields, aligned with previous findings (Ilie et al., 2017). The bounce-averaged drift coefficients were investigated based on such a imposed dawn-dusk inductive electric field, to reflect the effect of imposed electric field on the radial and azimuthal drift on different equatorial spatial locations. Next, we constructed a sharp Gaussian pulse with a certain azimuthal width, that propagates toward the Earth with a constant speed, starting around the outer boundary of numerical domain and peaking at midnight, similar with the ones proposed by Gabrielse, Harris, Angelopoulos, Artemyev, and Runov (2016); Li et al. (1998). As the pulse propagates inward, we observe local particles being swept earthward, physically from a location of lower magnetic field strength to that of higher magnetic field strength as the pulse propagates through, and being energized dramatically, as reflected by the resulting bounce-averaged energization rate coefficient. Finally, based on an analytical formulation of a time-changing magnetic field that starts as a dipole field and is being stretched toward the nightside tail while compressed inward on dayside, which then returns to the initial dipole state, we calculated the resulting inductive electric field on the magnetic equatorial plane as the magnetic field changes. In this case, we observe dawn-to-dusk inductive electric field during stretching process, and dusk-to-dawn inductive electric field during dipolarization. The corresponding drift and energization rate at different equatorial locations at different time moments will be presented and analyzed in later section.

2 Methodology

In this section we describe the kinetic drift model under which the numerical experiments are performed, and the new developments implemented in order to account for the effect of inductive electric fields. These include an introduction to the governing kinetic equation, along with the incorporation of the new terms that arose due to the presence of inductive electric fields. Furthermore, both the electric and magnetic field formulations within the model are described, to introduce the numerical experiments reported here, before analyzing (in later sections) the associated kinetic effects that arise due to temporal changes in the magnetic field.

2.1 Hot Electron-Ion Drift Integrator

The Hot Electron-Ion Drift Integrator (HEIDI) is an inner magnetosphere kinetic drift model that solves the time-dependent, gyration- and bounce-averaged Boltzmann equation for the equatorial phase-space distribution function $F(t, \mathbf{r}_0, \mathbf{v}_0)$ of five ring current species (e^-, H^+, He^+, N^+, O^+), that could be solved for individually, or collectively. The HEIDI model adopts an equatorial computation domain in space, discretized uniformly both in radial and azimuthal directions, and is capable of handling arbitrary electric and magnetic fields. The bounce-averaged kinetic equation solved by HEIDI is (Ilie, Liemohn, Toth, & Skoug, 2012; Liemohn, Ridley, Gallagher, Ober, & Kozyra, 2004):

$$\frac{\partial F}{\partial t} + \frac{1}{R_0^2}\frac{\partial}{\partial R_0}\left(R_0^2 \left\langle \frac{dR_0}{dt} \right\rangle F\right) + \frac{\partial}{\partial \phi_0}\left(\left\langle \frac{d\phi_0}{dt} \right\rangle F\right) + \frac{1}{\sqrt{W}}\frac{\partial}{\partial W}\left(\sqrt{W}\left\langle \frac{dW}{dt} \right\rangle F\right) + \frac{1}{h\left(\mu_0\right)\mu_0}\frac{\partial}{\partial \mu_0}\left(h\left(\mu_0\right)\mu_0 \left\langle \frac{d\mu_0}{dt} \right\rangle F\right) = \left\langle \frac{\delta F}{\delta t} \right\rangle_{collision} + \left\langle \frac{\delta F}{\delta t} \right\rangle_{source} \tag{1}$$

Equation 1 describes the time-evolution of the phase-space distribution function at a certain coordinate $(\mathbf{r}_0, \mathbf{v}_0)$ within the equatorial configuration-velocity space, under the effect of drifts (in both azimuthal and radial directions), energization, pitch-angle scattering, and various loss mechanisms. These losses currently include Coulomb collisions, charge exchange with the hydrogen geocorona, and precipitative losses to the upper atmosphere, all considering full pitch angle distributions. The four independent variables that constitute the equatorial phase-space distribution function F are $(\mathbf{r}_0, \mathbf{v}_0) = (R_0, \phi_0, W, \mu_0 = cos(\alpha_0))$, where R_0 represents the radial distance on the magnetic equatorial surface (defined by the location of magnetic field minima), ϕ_0 is the Magnetic Local Time (MLT), W denotes the species kinetic energy, and $\mu_0 = cos(\alpha_0)$ represents the cosine of the species equatorial pitch angle. In the HEIDI model, the equatorial configuration space covers all MLTs, and L shell values spanning from 2 to 6.5, while the velocity space covers all equatorial pitch angles and energies ranging from $10eV$ to $400keV$. The distribution function of any of the five species can be computed across the entire equatorial configuration-velocity space. The source term on the right hand side of Equation 1 is represented by the injection from the outer boundary of simulation domain on the nightside, based on particle flux data on the nightside outer boundary.

The large bracket $\langle\rangle$ in Equation 1 denotes the bounce-averaging operation, and for an arbitrary scalar quantity it is defined as (Roederer, 1970):

$$\langle A \rangle = \frac{1}{S_B}\int_{s_{m'}}^{s_m} \frac{A}{\sqrt{1 - \frac{B(s)}{B_m}}} ds \tag{2}$$

where s is the field line length measured from the ionospheric foot point along the field line, $B(s)$ denotes the magnetic field magnitude along the field line, B_m is the magnetic field at the mirror point locations (s_m and $s_{m'}$), which depend on the equatorial pitch-angle. To calculate the bounce-averaged quantities, HEIDI traces each individual field line whose equatorial intersection lays within the computation domain, and employs a field-aligned grid that discretizes each field line (starting and ending at the Earth's surface at certain magnetic foot-points) into a nonuniform field aligned grid (set to 101 points along the field line for this study), along which the numerical integrals are performed (Ilie et al., 2012). S_B is the half-bounce path length, calculated as:

$$S_B = \int_{s_{m'}}^{s_m} \frac{ds}{\sqrt{1 - \frac{B(s)}{B_m}}} \tag{3}$$

The parameter $h(\mu_0)$ in Equation 1 is related to the half-bounce period of trapped particles via:

$$h = \frac{1}{2R_0} \int_{s_{m'}}^{s_m} \frac{ds}{\sqrt{1 - \frac{B(s)}{B_m}}} = \frac{S_B}{2R_0} \tag{4}$$

In addition, the term $\left\langle \frac{dR_0}{dt} \right\rangle$ describes the radial component of the bounce-averaged total drift of a particular ion species,

$$\left\langle \frac{dR_0}{dt} \right\rangle = \hat{r}_0 \cdot \langle \mathbf{v}_{GC} \rangle + \hat{r}_0 \cdot \langle \mathbf{v}_{E\times B} \rangle \tag{5}$$

while the term $\left\langle \frac{d\phi_0}{dt} \right\rangle$ describes the azimuthal component of bounce-averaged total drift,

$$\left\langle \frac{d\phi_0}{dt} \right\rangle = \hat{\phi}_0 \cdot \langle \mathbf{v}_{GC} \rangle + \hat{\phi}_0 \cdot \langle \mathbf{v}_{E\times B} \rangle \tag{6}$$

In the above equations, the $\langle \mathbf{v}_{GC} \rangle$ denotes the bounce-averaged magnetic gradient-curvature drift of certain ion species along a specific closed magnetic field line that intersects the magnetic equatorial plane on a location sampled by HEIDI equatorial spatial grid. For an arbitrary magnetic field, the magnetic gradient-curvature drift is specified in HEIDI as (Ilie et al., 2012):

$$\mathbf{v}_{GC} = -\frac{m}{qB^4} \left(v_{\parallel}^2 + \frac{v_{\perp}^2}{2} \right) \left[\nabla \frac{B^2}{2} \times \mathbf{B} \right] \tag{7}$$

where q is the particle mass, and $v_{\parallel}$ and $v_{\perp}$ represent the particle's parallel and perpendicular velocity, respectively. The bounce-averaged $\mathbf{E} \times \mathbf{B}$ drift $\langle \mathbf{v}_{E\times B} \rangle$ is reduced to the local $\mathbf{E}_{0(total)} \times \mathbf{B}_0$ drift on the magnetic equatorial plane (Roederer, 1970), where $\mathbf{E}_{0(total)}$ is the total electric field on the magnetic equatorial plane, and $\mathbf{B}_0$ is the magnetic field at the same location. To account for the effect of inductive electric field in the HEIDI model, we decompose the total electric field into the inductive component and

electrostatic components ($\mathbf{E}_{total} = \mathbf{E}_i + \mathbf{E}_\Phi$) (Ilie et al., 2017), so that the bounce-averaged drift Equations 5 and 6 can be expanded as:

$$\left\langle \frac{dR_0}{dt} \right\rangle = \hat{r}_0 \cdot \langle \mathbf{v}_{GC} \rangle + \hat{r}_0 \cdot \langle \mathbf{v}_{E\times B} \rangle = \hat{r}_0 \cdot \langle \mathbf{v}_{GC} \rangle + \hat{r}_0 \cdot \frac{\mathbf{E}_{0(\Phi)} \times \mathbf{B}_0}{B_0^2} + \hat{r}_0 \cdot \frac{\mathbf{E}_{0(i)} \times \mathbf{B}_0}{B_0^2} \tag{8}$$

$$\left\langle \frac{d\phi_0}{dt} \right\rangle = \hat{\phi}_0 \cdot \langle \mathbf{v}_{GC} \rangle + \hat{\phi}_0 \cdot \langle \mathbf{v}_{E\times B} \rangle = \hat{\phi}_0 \cdot \langle \mathbf{v}_{GC} \rangle + \hat{\phi}_0 \cdot \frac{\mathbf{E}_{0(\Phi)} \times \mathbf{B}_0}{B_0^2} + \hat{\phi}_0 \cdot \frac{\mathbf{E}_{0(i)} \times \mathbf{B}_0}{B_0^2} \tag{9}$$

where $\mathbf{E}_{0(i)}$ and $\mathbf{E}_{0(\Phi)}$ denotes the equatorial inductive and electrostatic component of total electric field on magnetic equatorial plane, such that $\mathbf{E}_{0(total)} = \mathbf{E}_{0(i)} + \mathbf{E}_{0(\Phi)}$. The previous versions of HEIDI (Ilie et al., 2012; Liemohn et al., 2006; Ridley & Liemohn, 2002) did not consider the $\mathbf{E}\times\mathbf{B}$ drift driven by the inductive electric field $\mathbf{E}_i$, i.e., neglecting the equatorial inductive drift $\frac{\mathbf{E}_{0(i)}\times\mathbf{B}_0}{B_0^2}$, and treated the summation of magnetic gradient-curvature drift and $\mathbf{E}\times\mathbf{B}$ drift driven by the electrostatic field $\mathbf{E}_\Phi$ as the total drift. This electrostatic assumption can lead to a misleading estimation of the total drift, in addition to the energization rate of each ring current species, especially during times when the effect of inductive electric field $\mathbf{E}_i$ cannot be ignored, compared with the electrostatic field $\mathbf{E}_\Phi$. The red colored terms in Equations 8 and 9 account for the effects of the inductive electric field on the total particle drift, and constitutes one major new development that allows the inclusion of various inductive electric field models in HEIDI.

The term $\left\langle \frac{dW}{dt} \right\rangle$ describes the bounce-averaged energization rate along the drift path of a certain ion species,

$$\begin{aligned}\left\langle \frac{dW}{dt} \right\rangle = \frac{W}{B_0}\left(1-\frac{I}{2h}\right)\frac{\partial B_0}{\partial t} &+ W\left\langle \frac{dR_0}{dt} \right\rangle\left(\frac{1}{B_0}\left(1-\frac{I}{2h}\right)(\hat{r}_0\cdot\nabla B_0) - \frac{1}{h}\left(\frac{I}{R_0}+\hat{r}_0\cdot\nabla I\right)\right) \\ &+ W\left\langle \frac{d\phi_0}{dt} \right\rangle\left(\frac{1}{B_0}\left(1-\frac{I}{2h}\right)\left(\hat{\phi}_0\cdot\nabla B_0\right) - \frac{1}{h}\left(\hat{\phi}_0\cdot\nabla I\right)\right) - \frac{W}{h}\frac{\partial I}{\partial t}\end{aligned} \tag{10}$$

and the term $\left\langle \frac{d\mu_0}{dt} \right\rangle$ describes the bounce-averaged rate of change of the cosine of equatorial pitch-angle of a certain ion species,

$$\begin{aligned}\left\langle \frac{d\mu_0}{dt} \right\rangle = -\frac{\left(1-\mu_0^2\right) I}{2h\mu_0}\Bigg\{ &\left\langle \frac{dR_0}{dt} \right\rangle\left(\frac{1}{2B_0}(\hat{r}_0\cdot\nabla B_0) + \frac{1}{R_0} + \frac{1}{I}(\hat{r}_0\cdot\nabla B_0)\right) \\ &+ \left\langle \frac{d\phi_0}{dt} \right\rangle\left(\frac{1}{2B_0}\left(\hat{\phi}_0\cdot\nabla B_0\right) + \frac{1}{I}\left(\hat{\phi}_0\cdot\nabla I\right)\right) + \frac{1}{2B_0}\frac{\partial B_0}{\partial t} + \frac{1}{I}\frac{\partial I}{\partial t}\Bigg\}\end{aligned} \tag{11}$$

where the I quantity (which is also pitch-angle dependent) is related to the second adiabatic invariant via (Roederer, 1970):

$$I = \frac{1}{R_0}\int_{s_m}^{s_{m'}} ds \sqrt{1 - \frac{B(s)}{B_m}} \tag{12}$$

241 The red colored terms $\left\langle \frac{dR_0}{dt} \right\rangle$ and $\left\langle \frac{d\phi_0}{dt} \right\rangle$ in Equation 10 and Equation 11 highlight the
242 modified drift terms that take into account the effect of the inductive electric field. These
243 coefficients reflect the equatorial drift velocities of ring current particles, which are de-
244 pendent on both magnetic and electric field configurations. The coefficients $\left\langle \frac{dW}{dt} \right\rangle$ and
245 $\left\langle \frac{d\mu_0}{dt} \right\rangle$ reflect the rate of energy change and pitch-angle scattering of charged particles,
246 which in turn depend on the drift, electromagnetic field configurations, and explicitly
247 on the rate of temporal change of magnetic field ($\frac{\partial B_0}{\partial t}$). Modifications of the drift coef-
248 ficients have been implemented, to include the effect of the inductive electric field on the
249 drift dynamics of ring current. In the next section, we will examine the behavior of these
250 kinetic coefficients under different magnetic and electric field configurations.

251 2.2 Generalized Magnetic Field in HEIDI

During geomagnetically quiet times, the dipole magnetic field provides a reasonable approximation for the geomagnetic field in the near-Earth region. However, during storm times, the geomagnetic field is distorted by undergoing a compression on the dayside and stretching on the nightside. Therefore, in order to accurately model the particle transport and energization processes during storm time, a geomagnetic field model that is able to account for the distortion of magnetic field is needed. The HEIDI model has the appropriate formalism in place to account for arbitrary magnetic field configuration, therefore accounting for the distortion of geomagnetic field during storm time (Ilie et al., 2012). In order to assess the role of inductive electric fields to the overall particle drifts, we employ an idealized, analytic formulation of the magnetic field (which will be discussed in details next), constructed from a dipole magnetic field being distorted in the x direction by a set of stretching factors a and $b(t)$, that determine the extent of stretching, where a is a constant while $b(t)$ can be time-dependent, and specifies the MLT dependence of magnetic field (in such a way that the dipole field can be recovered from setting $a = 1$ and $b(t) = 0$). The choice of this realistic, yet analytic and intuitive magnetic field, not only allows us to easily test and validate the model, but also to assess how the time dependent magnetic field alters the particle drifts and contributes to their energization. The resulting magnetic field components, expressed in Cartesian coordinate system, are:

$$B_x(\mathbf{r}, t) = \frac{3zx}{(x^2\alpha^2(\phi, t) + y^2 + z^2)^{\frac{5}{2}}} \tag{13}$$

$$B_y(\mathbf{r},t) = \frac{3zy}{(x^2\alpha^2(\phi,t)+y^2+z^2)^{\frac{5}{2}}} \tag{14}$$

$$B_z(\mathbf{r},t) = \frac{2z^2-x^2\alpha^2(\phi,t)-y^2}{(x^2\alpha^2(\phi,t)+y^2+z^2)^{\frac{5}{2}}} \tag{15}$$

where $\alpha(\phi,t) = a+b(t)\cdot cos(\phi)$ is the stretching coefficient in terms of the set of stretching factors a and $b(t)$ introduced earlier, specifying extent of magnetic field being distorted in the x direction away from the dipole, and $\phi \in [0, 2\pi]$ represents the azimuthal angle. Such a magnetic field possesses the divergence-free nature regardless of the value of stretching factors a and b, therefore represents a physical field. The associated equation of magnetic field line is:

$$R = LR_E cos^2(\lambda)\sqrt{\alpha^2 cos^2(\lambda)cos^2(\phi) + cos^2(\lambda)sin^2(\phi) + sin^2(\lambda)} \tag{16}$$

where $\lambda \in [-\frac{\pi}{2}, \frac{\pi}{2}]$ is the magnetic latitude with 0 centered at the equator. The configuration of the magnetic field in 3D space is shown in Figure 1, which shows the magnetic field lines (with four different foot-points) at several MLTs, as the stretching factor b deviates from 0, meanwhile fixing stretching factor a as 1. The dark hemisphere represents the nightside, and the yellow hemisphere represents the dayside. The black lines ($a = 1, b = 0$) represent the dipole magnetic field lines (unstretched), the red lines ($a = 1, b = 0.4$) represent a heavily stretched case away from dipole, and the yellow lines ($a = 1, b = 0.2$) represent a moderately stretched case. It can be observed that the relative displacement of equatorial intersection of stretched field lines (with the same foot point) relative to the dipole is larger on the dayside ($x < 0$ region) than on the nightside ($x > 0$ region), which means that the magnitude of field intensification on the dayside is stronger than the magnitude of field attenuation on the nightside, for the non-dipolar configurations. By construction, the field lines at dawn and dusk remain dipolar regardless of the change of stretching factor. The exact radial distance of equatorial intersection of field lines with different food points under different stretching factors are attached in the Appendix.

Based on Equations 13 and 14, the equatorial ($z = 0$) B_x and B_y are vanishing regardless of the values set for stretching factors b. For equatorial B_z, there will be no MLT dependence for the dipole case ($a = 1$ and $b = 0$), implying that B_z possess perfect circular symmetry around the center of the Earth. As the dipole magnetic configuration is being distorted (by increasing the stretching factor b), magnetic field is intensified on dayside while weakened on nightside, compared with dipole configuration at the same location. More insight about the extent of distortion may be obtained by re-writing

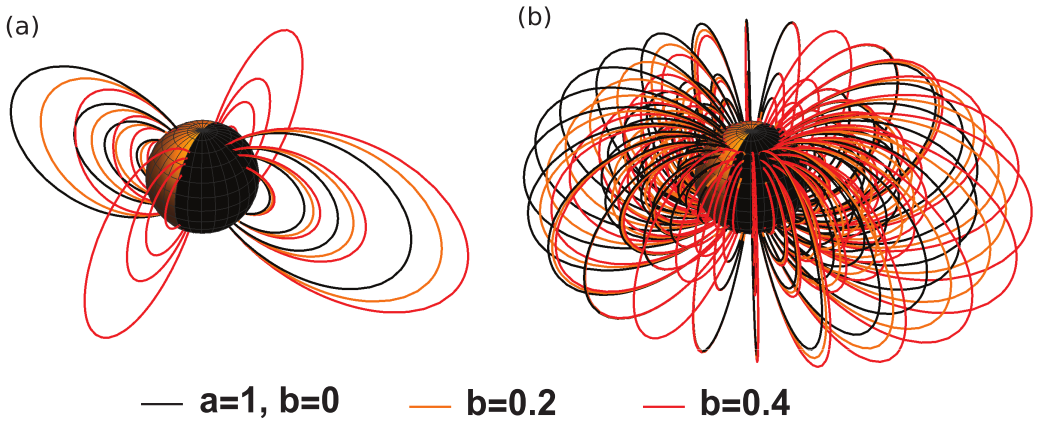

Figure 1. Magnetic field configuration under 3 different stretching factors, with foot-points of 30°, 45°, 52° and 60°. The black lines represents the dipole magnetic field lines, the red represents a heavily stretched case away from dipole, and the yellow represents a moderately stretched case. Panel (a) shows the field lines at midnight, noon, dawn and dusk, while panel (b) shows the field lines at multiple MLTs.

Equation 15 in spherical coordinates, then extracting the equatorial value ($B_z(z=0)$ or $B_z(\theta=\frac{\pi}{2})$, denoted as B_{z0}):

$$B_{z0}(\mathbf{r}_0,t) = \frac{1}{r^3}(\alpha^2(\phi,t)\cdot cos^2(\phi) + sin^2(\phi))^{-\frac{3}{2}} \tag{17}$$

From Equation 17, we obtain the ratio of equatorial B_z between stretched and dipole configuration to be:

$$\frac{B_{z0}(\mathbf{r}_0,t)}{B_{z0}^{dipole}(\mathbf{r}_0,t)} = (\alpha^2(\phi,t)\cdot cos^2(\phi) + sin^2(\phi))^{-\frac{3}{2}} \tag{18}$$

It can be observed from Equation 18 that the ratio is not dependent on radial distance, and as the stretching factor $b(t)$ grows larger, the ratio will be larger on dayside (corresponding to range $\frac{\pi}{2} < \phi < \frac{3\pi}{2}$) and smaller on nightside. To assess the extent of field distortion, we present in Figure 2 the ratio between stretched equatorial B_z and dipole equatorial B_z cases (in Log scale), in which panel (a), (b) and (c) shows the ratio of equatorial B_z for the $b = 0.1$, $b = 0.2$ and $b = 0.4$ cases, respectively, with the dipole equatorial B_z. The blue regions represent the depression of magnetic field, while the red regions represent the intensification of the magnetic field. The maximum intensification and depression of equatorial B_z is seen at noon and midnight, respectively, while the field remains at its dipole value at both dawn and dusk. Under the moderate stretched

case of $b = 0.2$, the equatorial B_z becomes 195% of that of the dipole equatorial B_z at noon and 58% at midnight, while under the severely stretched case of $b = 0.4$, the equatorial B_z becomes 463% of dipole equatorial B_z at noon and 36% at midnight. Consequently, the change of equatorial B_z is non-linear with the change of stretching factor b. Furthermore, the extent of magnetic field intensification on dayside is much larger than the extent of magnetic field depression on nightside, which is also verified by the difference on the relative displacement of stretched field lines on dayside and nightside, as reflected in Figure 1.

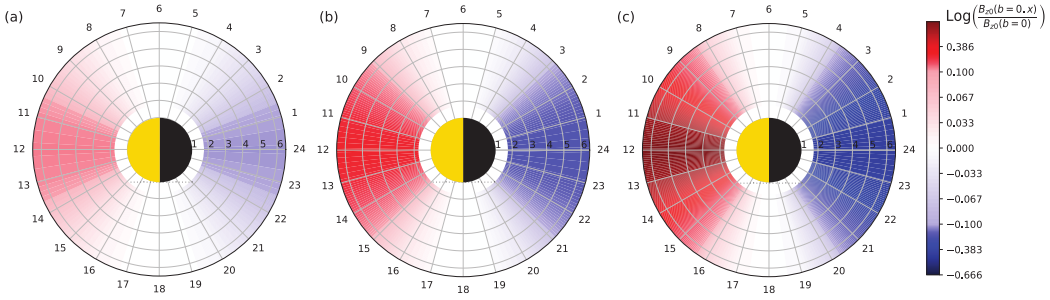

Figure 2. Equatorial B_z ratio between stretched field and dipole field. The value of x within b=0.x on the label of colorbar takes 0.1, 0.2 or 0.4, in such a way that panel (a), (b) and (c) shows the ratio of equatorial B_z for the $b = 0.1$, $b = 0.2$ and $b = 0.4$ cases, respectively, with the dipole equatorial B_z.

2.3 Analytical Inductive Electric Field Models

Until recently, the HEIDI model treated the superposition of the gradient-curvature drift and $\mathbf{E} \times \mathbf{B}$ drift driven by the electrostatic field $\mathbf{E}_\Phi$ as the total drift. This represents a reasonable assumption under quiet time conditions, when the magnetic field configuration changes very slowly or not at all, and the field can be treated as static. However, during storm time, when the magnetic field changes dramatically, the model is not able to capture the effect of temporal change of magnetic field. To address this issue, we have further developed the HEIDI model and added additional drift terms that arise in the presence of inductive electric fields, as described in Equations 8 and 9. The electric and magnetic field information is either obtained from another physics based model, such as an MHD model if executing in the coupled mode, or can be obtained from certain routine that sets up the field information within the drift kinetic model. To verify and test

the functionality of the model after including the effect of inductive electric field, we set up two simplified analytical inductive electric field models. In addition, we have developed a self-consistent electric model based on an arbitrary magnetic field configuration. The details on the inductive electric models are introduced and discussed next.

2.3.1 MLT Dependent Inductive Electric Field Model

Several studies reported that the substorm electric field in the near-Earch plasma sheet region has a magnitude around several mV/m, and the associated direction is mainly in the dawn-to-dusk direction (Antonova & Ganushkina, 1997; Holter et al., 1995; Matsui et al., 2003; Nishimura, Shinbori, Ono, Iizima, & Kumamoto, 2006; Pedersen et al., 1985), and drives many physical processes that are important for understanding the inner magnetosphere plasma dynamics. On the other hand, the large scale dawn-dusk electric field is set up by the interaction between solar wind and Earth's intrinsic magnetic field (therefore magnetic activity dependent) (Califf et al., 2014; Nishimura et al., 2009; Rowland & Wygant, 1998), driving charged particles toward the Earth from magnetotail. As plasma sheet particles are being convected Earthwards from weaker magnetic field to stronger magnetic field regions, they are adiabatically energized and contribute to the ring current hot ion populations.

Although the direction and magnitude of the magnetospheric electric field can be clearly measured, it is difficult to determine the magnitude and direction of the associated inductive component, since it cannot be separated from the measured total electric field at ease. However, since the inductive effect extends all over the space even though the temporal magnetic field is localized (Ilie et al., 2017), we can anticipate the inductive electric field produced by temporal change of magnetic field to have a global scale that extends over a broad spatial range within magnetosphere. As the first inductive electric field model in HEIDI, a simplistic equatorial dawn-dusk electric field that is MLT independent and distributes as a simple sine function of MLT, has been incorporated and tested. This represents a global (extends over several R_Es and lasts for hours) dawn-dusk inductive electric field, which allows us to quickly test the model and obtain an overview on the drift and energization rate associated with it. In addition, this global field can be understood as the inductive component of the electric field that arises dues to the continuous changes in the magnetic field at all time (Ilie et al., 2017). Mathematically, the

MLT-dependent dawn-dusk electric fields is constructed as:

$$\mathbf{E}_i(\mathbf{r}) = 3.6 sin(\phi)\hat{y}\frac{mV}{m} \tag{19}$$

and field distribution on the equatorial plane is showed in Figure 3.

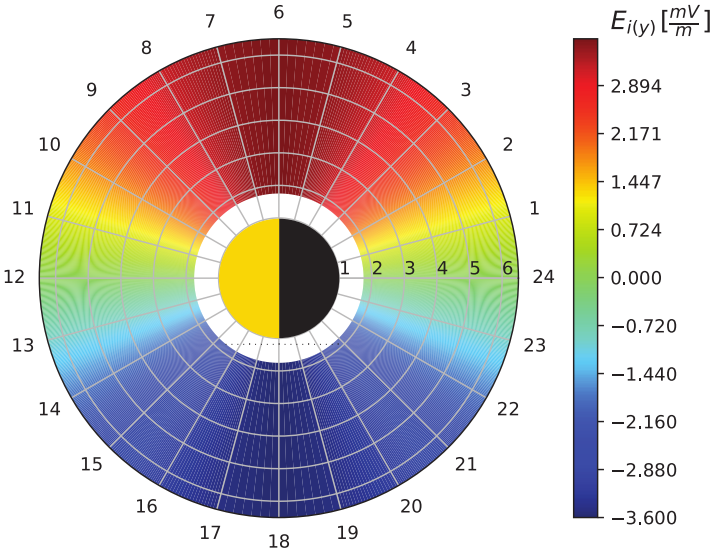

Figure 3. MLT dependent equatorial inductive electric field

2.3.2 Propagating Gaussian Pulse Inductive Electric Field Model

It has been widely observed that particle injections are quite common and intense around the onset of a magnetospheric substorm, associated with sudden increase in the particle flux in detectors of finite energy bandwidth across tens to hundreds keV (Birn et al., 1997; Gabrielse et al., 2012; Kivelson & Russell, 1995; Nakamura et al., 2013; Sarris et al., 2002). Such injections of energetic particle appear to be moving radially toward the Earth, and are often observed in a narrow region at or near local midnight (Belian, Baker, Higbie, & Hones Jr., 1978; Gabrielse et al., 2014; Lopez, Sibeck, McEntire, & Krimigis, 1990; Nakamura et al., 2002; Runov et al., 2009, 2011; V. A. Sergeev, Chernyaev, et al., 2012; Thomsen et al., 2001). The injection region has been modeled as a wave that propagates from the tail region into the inner magnetospheire, energizing and transporting plasma as it propagates through the space (Birn et al., 1998; Ganushkina, Amariutei, Shprits, & Liemohn, 2013; Ingraham et al., 2001; W. L. Liu et al., 2009; Mithaiwala & Horton, 2005). Models have been developed to simulate and explain such type

of intense injections by introducing a transient induced electric field pulse polarized in azimuthal direction, which is associated with the dipolarization process in the magnetotail. In most models, it follows the form of a pulse of localized radial and azimuthal extent, propagating from magnetotail toward the Earth (Angelopoulos et al., 2002; Ganushkina et al., 2013; Li et al., 1998; Li et al., 1993; Li, Sarris, Baker, Peterson, & Singer, 2003). The propagation speed of the pulse is not constant, but reported to be decreasing nonlinearly as it propagates radially toward the Earth (Moore, Arnoldy, Feynman, & Hardy, 1981; Russell & McPherron, 1973). Taking the variation of the pulse's Earthward propagation speed into account, some models assume it to follow a linear drop-off along the radial distance r, to simulate its deceleration in the near-Earth region (Ganushkina, Pulkkinen, & Fritz, 2005; Li et al., 2003; Sarris et al., 2002). Typically, such a propagating Gaussian pulse electric field on the equatorial plane, based on polar coordinate system (r, ϕ), in which $r = 0$ at the center of the Earth and ϕ represents MLT, can be formulated as (Gabrielse et al., 2016; Li et al., 1998):

$$\mathbf{E}_{i(pulse)}(\mathbf{r}, t) = -E_0 e^{-\xi^2}(1 + c_1 cos(\phi - \phi_0))^p \hat{\phi} \tag{20}$$

where $\xi(r, t) = [r - r_i + v(r)(t - t_a)]/d$ determines the location of the pulse peak as pulse propagates, and then decays in radial direction; $v(r)$ is the pulse propagation velocity as a function of radial distance between the Earth center and the pulse peak; d controls the radial width of the pulse; $c_1 > 0$ and $p > 0$ constants are associated with the MLT dependence of the pulse height, which reaches maximum at $\phi = \phi_0$; $t_a(\mathbf{r}) = (c_2 R_E/v_a)(1 - cos(\phi - \phi_0))$ represents the delay time of the pulse from the peak MLT position ϕ_0 to other MLTs; c_2 controls the magnetic of such delay; for simplicity, here v_a is assumed to be a constant, denoting the longitudinal propagation speed of pulse, however, it can also be scaled with distance; And r_i is a parameter that decides the radial position of the pulse peak at the moment of $t = t_a$.

In the HEIDI model, we reproduced the transient induced electric field as a time-dependent propagating Gaussian pulse with purely azimuthal component and constant propagation speed, in addition with width restriction on azimuthal direction, as:

$$\mathbf{E}_i(\mathbf{r}, t) = -E_0(1 + c_1 cos(\phi - \phi_0))^p e^{-\xi^2}(e^{-\phi_1^2} + e^{-\phi_2^2})\hat{\phi} \tag{21}$$

where $\phi_1(\phi) = \frac{\phi - \phi_0}{\phi_d}$ and $\phi_2(\phi) = \frac{\phi - \phi_0 - 2\pi}{\phi_d}$ determine the decay in azimuthal direction; ϕ_d controls the azimuthal width of the pulse. For testing purposes, we specifically set up $\phi_0 = 0°$ corresponding to midnight, $E_0 = 1.8\frac{mV}{m}$, $c_1 = 1$, $c_2 = 0$ implying zero

time delay, $a = \frac{1.5R_E}{1000}\frac{1}{s}$ and $b = 0$ implying a radial-independent propagation speed of $v(r) = \frac{1.5R_E}{1000}\frac{1}{s}$, $p = 1$, $r_i = 5R_E$, $d = 0.1R_E$, and $\phi_d = \frac{\pi}{2}$. Note that, by construction, the peak amplitude of the pulse matches the amplitude of the MLT dependent inductive electric field described prior. The initial pulse and the pulse passing through $3R_E$ is showed in Figure 4.

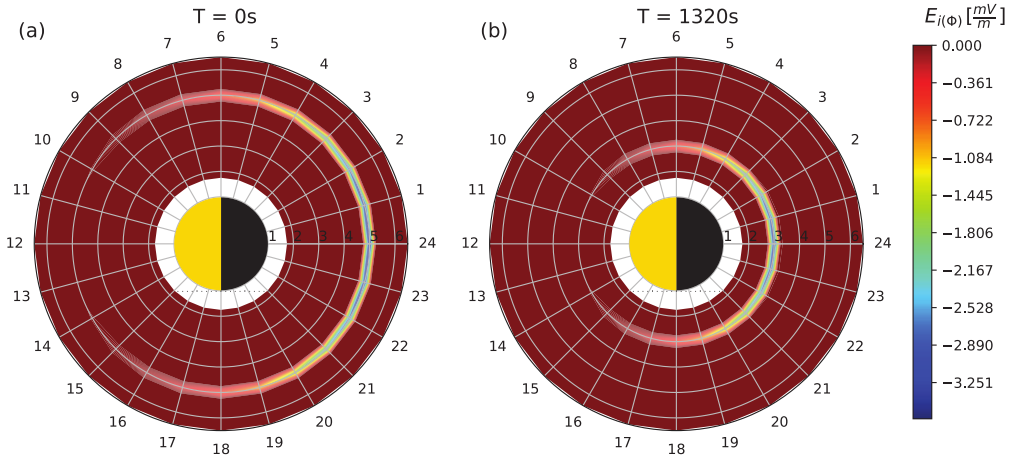

Figure 4. Earthward traveling Gaussian pulse electric field with pulse peak 3.6mV/m, at initial position (left) and passing through $3R_E$ (right). The deep blue shows the region around the pulse peak centered at midnight, propagating radially Earthward. The magnitude of the pulse decreases exponentially in the azimuthal direction away from the peak at midnight.

2.3.3 Self-Consistent Inductive Electric Field Model

The inclusion of self-consistent inductive electric field generated by the time-changing magnetic field, plays a critical role in obtaining a realistic description of magnetospheric convection in numerical models. However, the inclusion and calculation of the inductive component of the electric field in numerical models of the inner magnetosphere have been challenging (Toivanen, 2007; Zaharia et al., 2008). This paper presents an additional approach to include inductive effects, as an analytical approximation of inductive electric field based on a theoretical alternative for calculating the inductive electric field. This involves a full volume integration and removes the need to trace independent field lines.

2.3.4 Theoretical Description of Self-Consistent Inductive Electric Field

Any arbitrary vector $\mathbf{A}$ that is smoothly-varying in space can be expressed as the sum of an irrotational $\mathbf{A}_\Phi$ (which is curl-free) and a solenoidal component $\mathbf{A}_i$ (which is divergence-free), following the Helmholtz vector decomposition. Consequently, the total electric field $\mathbf{E}(\mathbf{r}, t)$ can be expressed as:

$$\mathbf{E}(\mathbf{r}, t) = \mathbf{E}_\Phi(\mathbf{r}, t) + \mathbf{E}_i(\mathbf{r}, t) \tag{22}$$

where $\mathbf{E}_i(\mathbf{r}, t)$ and $\mathbf{E}_\Phi(\mathbf{r}, t)$ are the solenoidal (divergence-free) and irrotational (curl-free) components of total electric field, respectively. The solution of such a solenoidal electric field is provided by (Ilie et al., 2017):

$$\mathbf{E}_i(\mathbf{r}, t) = \nabla \times \mathcal{E}(\mathbf{r}, t) = \frac{1}{4\pi}\frac{\partial}{\partial t}\int \frac{(\mathbf{r} - \mathbf{r}') \times \mathbf{B}(\mathbf{r}', t)}{|\mathbf{r} - \mathbf{r}'|^3} d^3\mathbf{r}' \tag{23}$$

which states that a change of magnetic field in time at an arbitrary location $\mathbf{r}'$ in space produces an inductive electric field at a location $\mathbf{r}$, implying that the effect of temporal change of magnetic field on producing inductive electric field extends all over space, even if the temporal change $\frac{\partial \mathbf{B}}{\partial t}$ is localized. Equation 23 provides a theoretical alternative to calculate the inductive electric field at a particular location in space, given the full magnetic field information as a function of space and time. However, such a volume integral does not always guarantee an analytical expression given an arbitrary magnetic field $\mathbf{B}(\mathbf{r}, t)$, and therefore requires either analytical or numerical approximation. In this paper we present an analytical approximation to the volume integral and the associated discretization of the computational domain, and the truncation of the integration range.

2.3.5 Numerical Implementation of Self-Consistent Inductive Electric Field

The calculation of self-consistent inductive electric field involves a volume integral about $\frac{\partial \mathbf{B}}{\partial t}$ as shown in Equation 23. Here, we introduce an analytical approximation of the volume integral associated with self-consistent inductive electric field calculation, using the analytical expression of the magnetic field model. From Equation 23, we can express the x-, y-, and z-components of the self-consistent inductive electric field as:

$$E_{i(x)}(\mathbf{r}, t) = \hat{x} \cdot \frac{1}{4\pi}\frac{\partial}{\partial t}\int \frac{(\mathbf{r} - \mathbf{r}') \times \mathbf{B}(\mathbf{r}', t)}{|\mathbf{r} - \mathbf{r}'|^3} d^3\mathbf{r}' := \frac{1}{4\pi}\frac{\partial}{\partial t} I_x(\mathbf{r}, t) \tag{24}$$

$$E_{i(y)}(\mathbf{r},t) = \hat{y} \cdot \frac{1}{4\pi}\frac{\partial}{\partial t}\int \frac{(\mathbf{r}-\mathbf{r}')\times \mathbf{B}(\mathbf{r}',t)}{|\mathbf{r}-\mathbf{r}'|^3} d^3\mathbf{r}' := \frac{1}{4\pi}\frac{\partial}{\partial t} I_y(\mathbf{r},t) \tag{25}$$

$$E_{i(z)}(\mathbf{r},t) = \hat{z} \cdot \frac{1}{4\pi}\frac{\partial}{\partial t}\int \frac{(\mathbf{r}-\mathbf{r}')\times \mathbf{B}(\mathbf{r}',t)}{|\mathbf{r}-\mathbf{r}'|^3} d^3\mathbf{r}' := \frac{1}{4\pi}\frac{\partial}{\partial t} I_z(\mathbf{r},t) \tag{26}$$

where $I_x(\mathbf{r},t)$, $I_y(\mathbf{r},t)$ and $I_z(\mathbf{r},t)$ denote the integral expression associated with each of the three components of the inductive electric field, expressed as:

$$I_x(\mathbf{r},t) := \int \frac{B_z(\mathbf{r}',t)(y - r'sin(\theta')sin(\phi')) - B_y(\mathbf{r}',t)(z - r'cos(\theta'))}{[(x - r'sin(\theta')cos(\phi'))^2 + (y - r'sin(\theta')sin(\phi'))^2 + (z - r'cos(\theta'))^2]^{\frac{3}{2}}} d^3\mathbf{r}' \tag{27}$$

$$I_y(\mathbf{r},t) := \int \frac{B_x(\mathbf{r}',t)(z - r'cos(\theta')) - B_z(\mathbf{r}',t)(x - r'sin(\theta')cos(\phi'))}{[(x - r'sin(\theta')cos(\phi'))^2 + (y - r'sin(\theta')sin(\phi'))^2 + (z - r'cos(\theta'))^2]^{\frac{3}{2}}} d^3\mathbf{r}' \tag{28}$$

$$I_z(\mathbf{r},t) := \int \frac{B_y(\mathbf{r}',t)(x - r'sin(\theta')cos(\phi')) - B_x(\mathbf{r}',t)(y - r'sin(\theta')sin(\phi'))}{[(x - r'sin(\theta')cos(\phi'))^2 + (y - r'sin(\theta')sin(\phi'))^2 + (z - r'cos(\theta'))^2]^{\frac{3}{2}}} d^3\mathbf{r}' \tag{29}$$

Note that the integral limit goes from zero to infinity (therefore covering the entire range of space) to represent the exact analytical integral result. However, the computational domain within numerical models has to be bounded, meaning that at a certain measurement point we could only evaluate the inductive electric field contributed from a finite volume. Assuming we set the center of the Earth to be origin, and we evaluate the inductive electric field contributed by $\frac{\partial \mathbf{B}}{\partial t}$ within a certain spherical shell region with inner radius R_a and outer radius R_b, then the three integrals become:

$$I_x(\mathbf{r},t) = \int_0^{2\pi}\int_0^{\pi}\int_{R_a}^{R_b} \frac{r'^2 sin(\theta')[B_z(\mathbf{r}',t)(y - r'sin(\theta')sin(\phi')) - B_y(\mathbf{r}',t)(z - r'cos(\theta'))]}{[(x - r'sin(\theta')cos(\phi'))^2 + (y - r'sin(\theta')sin(\phi'))^2 + (z - r'cos(\theta'))^2]^{\frac{3}{2}}} dr'd\theta'd\phi' \tag{30}$$

$$I_y(\mathbf{r},t) = \int_0^{2\pi}\int_0^{\pi}\int_{R_a}^{R_b} \frac{r'^2 sin(\theta')[B_x(\mathbf{r}',t)(z - r'cos(\theta')) - B_z(\mathbf{r}',t)(x - r'sin(\theta')cos(\phi'))]}{[(x - r'sin(\theta')cos(\phi'))^2 + (y - r'sin(\theta')sin(\phi'))^2 + (z - r'cos(\theta'))^2]^{\frac{3}{2}}} dr'd\theta'd\phi' \tag{31}$$

$$I_z(\mathbf{r},t) = \int_0^{2\pi}\int_0^{\pi}\int_{R_a}^{R_b} \frac{r'^2 sin(\theta')[B_y(\mathbf{r}',t)(x - r'sin(\theta')cos(\phi')) - B_x(\mathbf{r}',t)(y - r'sin(\theta')sin(\phi'))]}{[(x - r'sin(\theta')cos(\phi'))^2 + (y - r'sin(\theta')sin(\phi'))^2 + (z - r'cos(\theta'))^2]^{\frac{3}{2}}} dr'd\theta'd\phi' \tag{32}$$

where θ' denotes the zenith angle of source point, ϕ' the azimuthal angle of source point, and r' the radial distance of source point from the center of the Earth, as defined by the standard spherical coordinate system.

Although the analytical expressions of three integrals are obtained, it is difficult to directly evaluate each of them analytically, due to the exhaustive complexity of each of the magnetic field component $B_x(\mathbf{r},t)$, $B_y(\mathbf{r},t)$ and $B_z(\mathbf{r},t)$, given by Equation 13, 14 and 15, respectively. In this paper, we present a methodology to obtain an analytical approximation of these integrals based on spatial discretization. We discretize the

source point contribution shell region occupied by $r' \in [R_a, R_b]$, $\theta' \in [0, \pi]$ and $\phi' \in [0, 2\pi]$, with N_R being the number of radial grid points, N_θ being the number of zenith grid points in each fixed radial distance and azimuthal angle, and N_ϕ being the number of azimuthal grid points in each fixed radial distance and zenith angle, therefore forming a total number of $(N_R - 1) \times (N_\theta - 1) \times (N_\phi - 1)$ spherical patches. The magnetic field value could be evaluated at any grid point at any time moment, using the generalized magnetic field formulation in the HEIDI model. Here, we provide an illustration of an extremely coarse spherical grid (in 3D) shown in Figure 5, in which the grey dashed lines depict the grid configuration, and the black solid lines represent a set of dipole magnetic field lines shown for reference. Notice that the spherical grid is not field-aligned, and independent with the field lines stretching. The grid size in the illustration shown in Figure 5 is $\Delta R = 1.5R_E$, $\Delta\theta = \frac{\pi}{8}$ and $\Delta\phi = \frac{\pi}{4}$, which is much coarser than the grid employed in producing converged result (which is $\Delta R = 0.12R_E$, $\Delta\theta = \frac{\pi}{60}$ and $\Delta\phi = \frac{\pi}{90}$). Therefore, the grid structure in Figure 5 is just for illustration purposes, and does not represent the size of grid used in the computation. The decision of the proper grid size that produces reliable results will be described in Section 2.3.6.

Based on this discretization, the entire spatial volume integral presented in Equation 30, 31 and 32 could be approximated as the summation of the spatial volume integral over each individual spherical patch. Next, we locally approximate the integrand functions over which the spatial volume integral is performed, into polynomial functions, by expanding it around a local approximation point $(r'_0, \theta'_0, \phi'_0)$ in space, using Taylor expansion. In this case we adopted second-order Taylor expansion as described below:

$$\begin{aligned} f_i^n(r', \theta', \phi') \approx f_i^n(r'_0, \theta'_0, \phi'_0) + (r' - r'_0)\frac{\partial f_i^n}{\partial r'}(r'_0, \theta'_0, \phi'_0) + (\theta' - \theta'_0)\frac{\partial f_i^n}{\partial \theta'}(r'_0, \theta'_0, \phi'_0) \\ +(\phi' - \phi'_0)\frac{\partial f_i^n}{\partial \phi'}(r'_0, \theta'_0, \phi'_0) + \frac{1}{2}\Big[(r' - r'_0)^2\frac{\partial^2 f_i^n}{\partial r'^2}(r'_0, \theta'_0, \phi'_0) + (\theta' - \theta'_0)^2\frac{\partial^2 f_i^n}{\partial \theta'^2}(r'_0, \theta'_0, \phi'_0) \\ +(\phi' - \phi'_0)^2\frac{\partial^2 f_i^n}{\partial \phi'^2}(r'_0, \theta'_0, \phi'_0)\Big] + (r' - r'_0)(\theta' - \theta'_0)\frac{\partial^2 f_i^n}{\partial r' \partial \theta'}(r'_0, \theta'_0, \phi'_0) \\ +(r' - r'_0)(\phi' - \phi'_0)\frac{\partial^2 f_i^n}{\partial r' \partial \phi'}(r'_0, \theta'_0, \phi'_0) + (\theta' - \theta'_0)(\phi' - \phi'_0)\frac{\partial^2 f_i^n}{\partial \theta' \partial \phi'}(r'_0, \theta'_0, \phi'_0) \end{aligned} \tag{33}$$

where the superscript n represents the time-step index, and subscript $i \in \{x, y, z\}$ represents the spatial component index. Each f_i^n is defined to be the integrand function within each spatial volume integral at certain time step:

$$f_x^n(r', \theta', \phi') := r'^2 sin(\theta') \frac{B_z(\mathbf{r}', t_n)(y - r'sin(\theta')sin(\phi')) - B_y(\mathbf{r}', t_n)(z - r'cos(\theta'))}{[(x - r'sin(\theta')cos(\phi'))^2 + (y - r'sin(\theta')sin(\phi'))^2 + (z - r'cos(\theta'))^2]^{\frac{3}{2}}} \tag{34}$$

$$f_y^n(r',\theta',\phi') := r'^2 sin(\theta') \frac{B_x(\mathbf{r}',t_n)(z-r'cos(\theta')) - B_z(\mathbf{r}',t_n)(x-r'sin(\theta')cos(\phi'))}{[(x-r'sin(\theta')cos(\phi'))^2 + (y-r'sin(\theta')sin(\phi'))^2 + (z-r'cos(\theta'))^2]^{\frac{3}{2}}} \tag{35}$$

$$f_z^n(r',\theta',\phi') := r'^2 sin(\theta') \frac{B_y(\mathbf{r}',t_n)(x-r'sin(\theta')cos(\phi')) - B_x(\mathbf{r}',t_n)(y-r'sin(\theta')sin(\phi'))}{[(x-r'sin(\theta')cos(\phi'))^2 + (y-r'sin(\theta')sin(\phi'))^2 + (z-r'cos(\theta'))^2]^{\frac{3}{2}}} \tag{36}$$

As a result, each spatial volume integral presented in Equation 30, 31 and 32 could be approximated as:

$$I_i(\mathbf{r},t_n) \approx \sum_{i=1}^{N_R-1}\sum_{j=1}^{N_\theta-1}\sum_{k=1}^{N_\phi-1}\int_{\phi_k}^{\phi_{k+1}}\int_{\theta_j}^{\theta_{j+1}}\int_{R_i}^{R_{i+1}} f_i^n(r',\theta',\phi')dr'd\theta'd\phi' \tag{37}$$

If we expand each integrand function f_i^n within each discretized grid cell around the cell center, i.e. choosing $r'_0 = \frac{R_{i+1}+R_i}{2}$, $\theta'_0 = \frac{\theta_{j+1}+\theta_j}{2}$ and $\phi'_0 = \frac{\phi_{k+1}-\phi_k}{2}$, where $i \in [1, N_R-1]$, $j \in [1, N_\theta-1]$ and $k \in [1, N_\phi-1]$, then integrating over all the odd order terms returns 0, and what is left are only even order terms:

$$\begin{aligned} I_i(\mathbf{r},t_n) \approx \sum_{i=1}^{N_R-1}\sum_{j=1}^{N_\theta-1}\sum_{k=1}^{N_{\phi-1}}\int_{\phi_k}^{\phi_{k+1}}\int_{\theta_j}^{\theta_{j+1}}\int_{R_i}^{R_{i+1}}\Big[f_i^n(r'_0,\theta'_0,\phi'_0) + \frac{1}{2}((r'-r'_0)^2\frac{\partial^2 f_i^n}{\partial r'^2}(r'_0,\theta'_0,\phi'_0) \\ +(\theta'-\theta'_0)^2\frac{\partial^2 f_i^n}{\partial \theta'^2}(r'_0,\theta'_0,\phi'_0) + (\phi'-\phi'_0)^2\frac{\partial^2 f_i^n}{\partial \phi'^2}(r'_0,\theta'_0,\phi'_0))\Big]dr'd\theta'd\phi' \end{aligned} \tag{38}$$

The result of such a integral over a polynomial function could be analytically expressed as:

$$\begin{aligned} I_i(\mathbf{r},t_n) \approx \sum_{i=1}^{N_R-1}\sum_{j=1}^{N_\theta-1}\sum_{k=1}^{N_{\phi-1}}\Big\{ & f_i^n(r'_0,\theta'_0,\phi'_0)(R_{i+1}-R_i)(\theta_{j+1}-\theta_j)(\phi_{k+1}-\phi_k) \\ & +\frac{1}{6}\frac{\partial^2 f_i^n}{\partial r'^2}(r'_0,\theta'_0,\phi'_0)(\theta_{j+1}-\theta_j)(\phi_{k+1}-\phi_k)\Big[(R_{i+1}-r'_0)^3-(R_i-r'_0)^3\Big] \\ & +\frac{1}{6}\frac{\partial^2 f_i^n}{\partial \theta'^2}(r'_0,\theta'_0,\phi'_0)(R_{i+1}-R_i)(\phi_{k+1}-\phi_k)\Big[(\theta_{j+1}-\theta'_0)^3-(\theta_j-\theta'_0)^3\Big] \\ & +\frac{1}{6}\frac{\partial^2 f_i^n}{\partial \phi'^2}(r'_0,\theta'_0,\phi'_0)(R_{i+1}-R_i)(\theta_{j+1}-\theta_j)\Big[(\phi_{k+1}-\phi'_0)^3-(\phi_k-\phi'_0)^3\Big]\Big\} \end{aligned} \tag{39}$$

Finally the inductive electric field at each point in space is evaluated using the backward finite difference approximation in time on the integral result:

$$E_{i(x)}(\mathbf{r},t_n) \approx \frac{1}{4\pi}\frac{I_x(\mathbf{r},t_n)-I_x(\mathbf{r},t_{n-1})}{\Delta t} \tag{40}$$

$$E_{i(y)}(\mathbf{r},t_n) \approx \frac{1}{4\pi}\frac{I_y(\mathbf{r},t_n)-I_y(\mathbf{r},t_{n-1})}{\Delta t} \tag{41}$$

$$E_{i(z)}(\mathbf{r},t_n) \approx \frac{1}{4\pi}\frac{I_z(\mathbf{r},t_n)-I_z(\mathbf{r},t_{n-1})}{\Delta t} \tag{42}$$

where the time index $n \geq 2$, so the evaluation of inductive electric field on each measurement point starts from the second time step. The magnetic field at the first time step is usually initialized as dipole field.

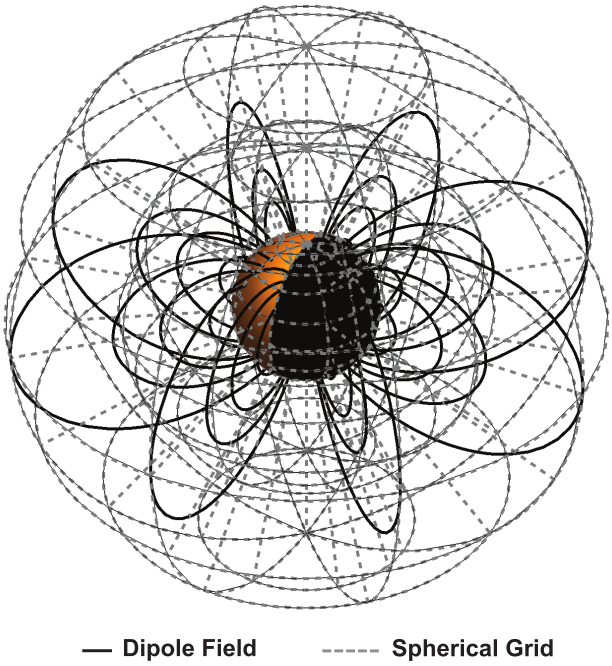

Figure 5. Illustration of an example uniform spherical grid structure in 3D. The grey dashed lines show the grid structure, and the black solid lines represent the dipole field lines with footpoint at 30°,45°,52° and 60° latitude. This is a sample grid for ΔR=1.5R_E, $\Delta\theta$=$\frac{\pi}{8}$ and $\Delta\phi$=$\frac{\pi}{4}$. The spherical grid is not field-aligned, therefore independent with the field lines stretching.

2.3.6 Equatorial Self-Consistent $\mathbf{E}_i$*: Convergence Test*

With the spherical grid setup introduced in previous section, we are employing uniform discretization in each direction, meaning that $R_{i+1} - R_i = \Delta R = \frac{R_b - R_a}{N_R - 1}$, $\theta_{j+1} - \theta_j = \Delta\theta = \frac{\pi}{N_\theta - 1}$ and $\phi_{k+1} - \phi_k = \Delta\phi = \frac{2\pi}{N_\phi}$, for all $i \in [1, N_R - 1]$, $j \in [1, N_\theta - 1]$ and $k \in [1, N_\phi - 1]$. The radial integration range is set to be $R_a = 2R_E$ and $R_b = 7R_E$, meaning that we only consider the contribution of $\frac{\partial \mathbf{B}}{\partial t}$ within a spherical shell of inner radius $R_a = 2R_E$ and outer radius $R_b = 7R_E$. In addition, tests (with full simulation time of 2000s) are performed under the specification of time-dependent stretching factor $b(t)$ to be:

$$b(t) = 0.05 \left| sin(\frac{\pi}{1000} t) \right| \tag{43}$$

with a set of four reference time moments t_1, t_2, t_3 and t_4 shown in Figure 6. The black curves represents the variation of stretching factor $b(t)$ within the full length of simulation time, and four colored vertical lines label the four reference time moments, which

are: $t_1 = 40s$ around the beginning of stretching, $t_2 = 400s$ around the end of stretching, $t_3 = 640s$ around the beginning of dipolarization, and $t_4 = 960s$ around the end of dipolarization.

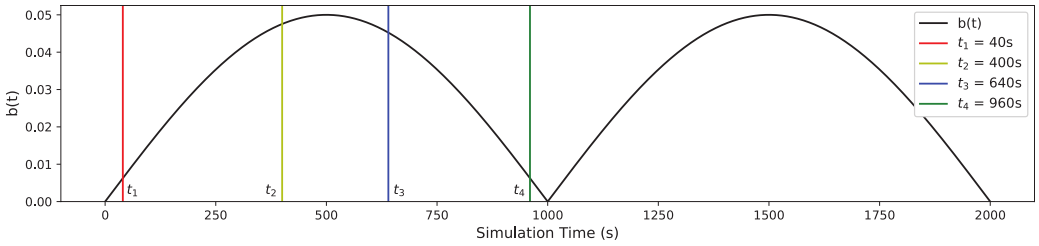

Figure 6. Plot of time variation of stretching factor $b(t)$ (black). The colored verticle lines label the four reference time moments: $t_1 = 40s$ the beginning of stretching, $t_2 = 400s$ the end of stretching, $t_3 = 640s$ the beginning of dipolarizing and $t_4 = 960s$ the end of dipolarizing.

To decide a set of proper number of grid points (N_R, N_ϕ, N_θ) that produces converged integration results, which do not change significantly if further increasing the number of grid points in every direction, we performed a convergence test by increasing the grid points (N_R, N_ϕ, N_θ) and compared the relative change of the integral results, and the results indicate that $(N_R, N_\phi, N_\theta) = (51, 120, 46)$ is a desired set of grid points. Figure 7 shows the relative change of calculated $|\mathbf{E}_i|$ (captured at $t_2 = 400s$) to the desired set of grid point (51,120,46), from a low resolution grid set (panel (a)) and a high resolution grid set (panel (b)). The maximum relative change from low resolution grid set (which is (21,24,13)) to the desired converged grid set is 4.78%, while decreases to 0.72% from high resolution grid set (which is (101,360,91)), which means that the equatorial $\mathbf{E}_i$ result does not change significantly if we further refine the grid from our chosen converged grid set (51,120,46). Such a direct integration method for computing self-consistent inductive electric field is computationally expensive, as it requires calculating the integral within every grid cell, for each single measurement point. The total computation time taken to complete the 2000s simulation is around 1200s, 16100s and 95880s for the set of number of grid point $(N_R, N_\phi, N_\theta) = (21, 24, 13)$, (51,120,46) and (101,360,91), respectively (without any parallel computing setups), corresponding to total number of grid cells of 5760, 270000 and 3240000. Because the equatorial self-consistent inductive electric field results changes only 0.72% at most as we further refine the grid from $(N_R, N_\phi, N_\theta) = (51, 120, 46)$ to a even higher resolution of $(N_R, N_\phi, N_\theta) = (101, 360, 91)$ (as showed in

Figure 7), but the computation time increases by a factor of 5 (from 16100s to 95880s), we regard the set of grid point $(N_R, N_\phi, N_\theta) = (51, 120, 46)$ as the converging grid set (and use it for result analysis), instead of going to an even finer grid.

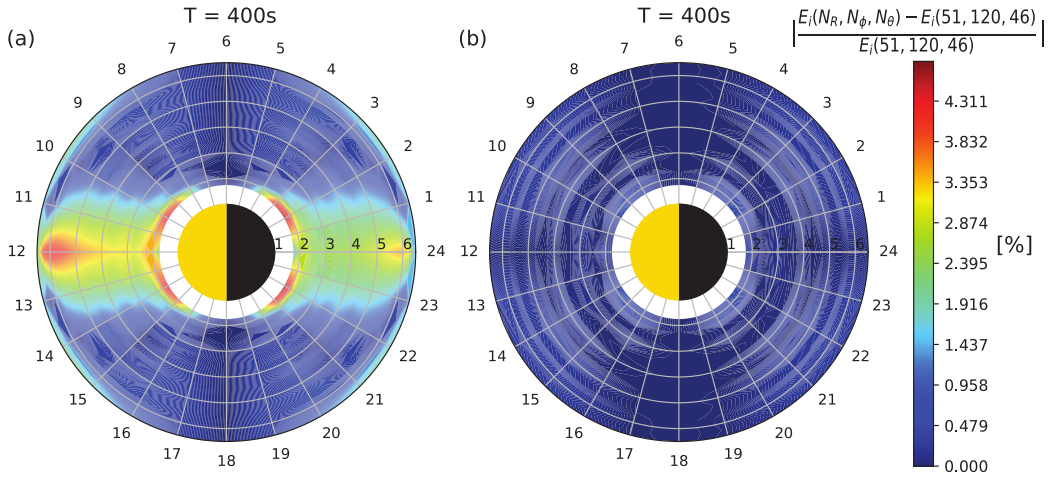

Figure 7. Convergence test of self-consistent equatorial $\mathbf{E}_i$, captured at $t_2 = 400s$. Panel (a) shows the plot of relative $|\mathbf{E}_i|$ change from (N_R, N_ϕ, N_θ)=(21,24,13) to (51,120,46), and panel (b) shows the relative $|\mathbf{E}_i|$ change from (N_R, N_ϕ, N_θ)=(51,120,46) to (101,360,91), both in the same scale. The maximum relative change (with respect to converged set (51,120,46)) in panel (a) is 4.78%, and decreases to 0.72% in panel (b).

The x and y components of equatorial inductive electric field (denoted as $E_{i(x)}$ and $E_{i(y)}$, respectively) at the four different time moments t_1, t_2, t_3 and t_4 are presented in Figures 8 and 9, respectively. $E_{i(x)}$ is vanishing around both midnight and noon, as showed in Figure 8, implying that $E_{i(y)}$ will be dominating around midnight and noon. $E_{i(y)}$ is only vanishing around dawn and dusk, due to the fact that dawn/dusk magnetic field is not changing with time (by construction). Both $E_{i(x)}$ and $E_{i(y)}$ reverse the sign as the magnetic field switches from stretching to dipolarizing and vice versa, meaning that the direction of drift caused by the equatorial inductive electric field is also reversed. This effect is not captured by any pre-defined inductive electric field models, as the ones previously described in Section 2.3.1 and Section 2.3.2. Furthermore, the magnitude of $E_{i(x)}$ and $E_{i(y)}$ at t_2 and t_3 are much smaller than the ones at t_1 and t_4, in correspondence with the relative equatorial $\frac{\partial B_0}{\partial t}$ at the four moments, which will be discussed later. The z component of equatorial inductive electric field is the trivial component, due to the fact

that B_x and B_y are very small in the region around equatorial plane, from where the most dominant source of equatorial inductive electric field (which is $\frac{\partial \mathbf{B}}{\partial t}$) resides.

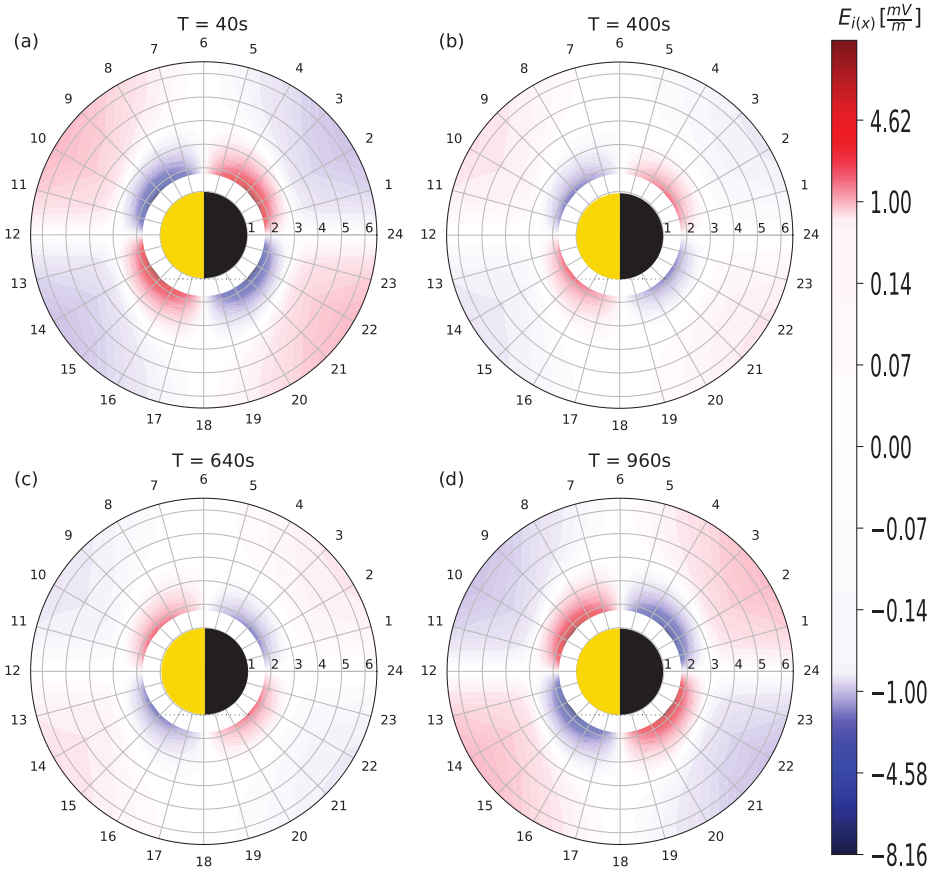

Figure 8. Equatorial $E_{i(x)}$ at the four time moments: (a) $t_1 = 40s$, (b) $t_2 = 400s$, (c) $t_3 = 640s$ and (d) $t_4 = 960s$.

Figure 10 shows the equatorial $\frac{\partial B_0}{\partial t}$ at the four moments. During the stretching period ($0 \leq t \leq 500s$), magnetic field is intensified on dayside while attenuated on nightside, corresponding to the distribution pattern in panel (a) and (b), and the reverse is true during the dipolarization period ($500s \leq t \leq 1000s$), corresponding to the distribution pattern in panel (c) and (d). Dawn/dusk equatorial $\frac{\partial B_0}{\partial t}$ is 0 all the time, and the magnitude around the turning moment (500s) is much smaller than the one at beginning of stretching and end of dipolarization. Figure 11 shows the equatorial $|\mathbf{E}_i|$ at the four moments. The magnitude is symmetric around the moment when the magnetic field switches from stretching to dipolarization ($t = 500s$), so the magnetic field topology in panel (a) and (d) is about the same as the one in (b) and (c), respectively, though the

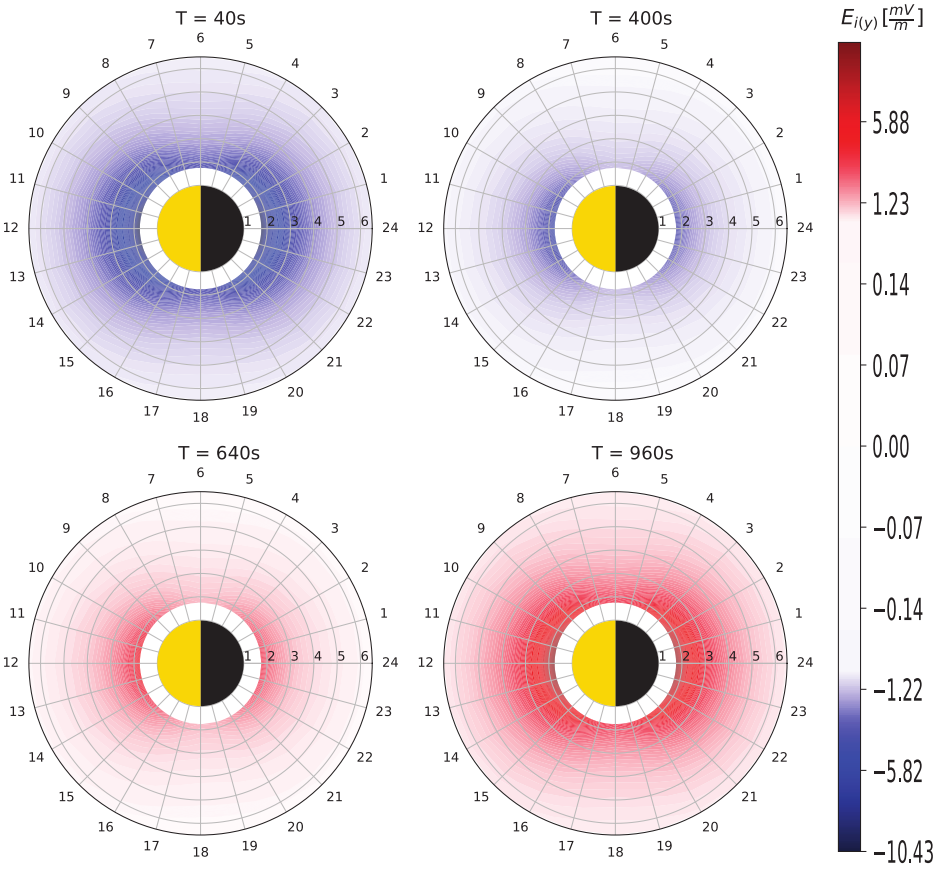

Figure 9. Equatorial $E_{i(y)}$ at the four time moments: (a) $t_1 = 40s$, (b) $t_2 = 400s$, (c) $t_3 = 640s$ and (d) $t_4 = 960s$.

direction is reversed. From Equation 23, we may expect that the inductive electric field would follow similar spatial distribution with $\frac{\partial \mathbf{B}}{\partial t}$. Although the inductive electric field at specific measurement point has to consider the contribution of $\frac{\partial \mathbf{B}}{\partial t}$ from everywhere in space, it is the $\frac{\partial \mathbf{B}}{\partial t}$ at the location around the measurement point $\mathbf{r}$ that contributes the most to the inductive electric field at $\mathbf{r}$, since it follows a $\frac{1}{|\mathbf{r}-\mathbf{r}'|^2}$ relation. Consequently, we may expect that the magnitude of equatorial inductive electric field distribution at a certain time moment to be similar with the distribution of equatorial $\frac{\partial B_0}{\partial t}$ at the same time moment, but not necessarily the same.

Comparison of the equatorial $\frac{\partial B_0}{\partial t}$ showed in Figure 10 with the magnitude of equatorial inductive electric field showed in Figure 11, indicates that they follow similar spatial distribution, and when equatorial $\frac{\partial B_0}{\partial t}$ is small, the corresponding equatorial $\mathbf{E}_i$ is also small. Consequently, the self-consistent equatorial $|\mathbf{E}_i|$ around dawn and dusk is weak

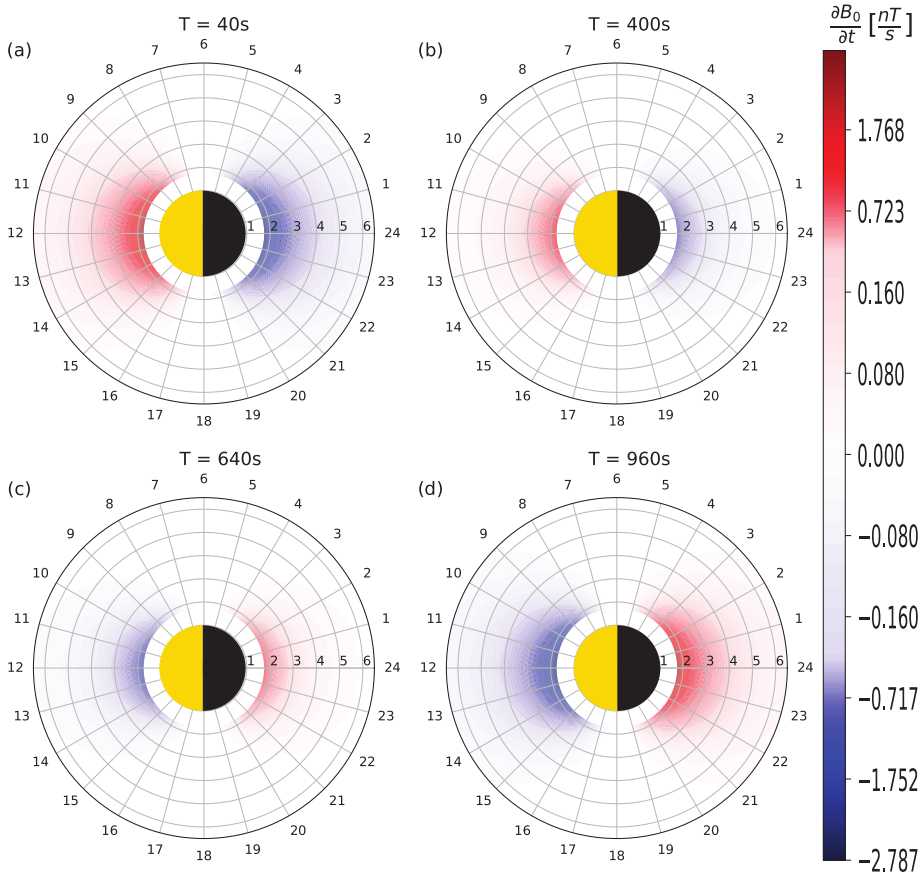

Figure 10. Equatorial $\frac{\partial B_0}{\partial t}$ atat the four time moments: (a) $t_1 = 40s$, (b) $t_2 = 400s$, (c) $t_3 = 640s$ and (d) $t_4 = 960s$.

compared with the one around midnight and noon, corresponding to associated equatorial $\frac{\partial B_0}{\partial t}$ distribution. Besides the equatorial $\frac{\partial \mathbf{B_0}}{\partial t}$, the temporal changes of magnetic field in regions right above and below the equatorial plane also contribute greatly to the inductive electric field on the equatorial plane. To better visualize the self-consistent inductive electric field vector in the equatorial plane, Figure 12 shows the vector $\mathbf{E}_i$ at $3.5R_E$. During the stretching period ($0 \leq t \leq 500s$), the inductive electric field points from dawn to dusk, as illustrated in panel (a) and (b), meaning that it has an effect of driving particles Earthward on the nightside, while away from the Earth on the dayside. During the dipolarization period ($500s \leq t \leq 1000s$), the inductive electric field points from dusk to dawn, as showed in panel (c) and (d), so the effect of inductive drift is reversed (since the direction of $\mathbf{E}_i$ is reversed). Furthermore, we can see that it is mostly solenoidal, as expected due to its divergence-free nature. Additional quantitative descrip-

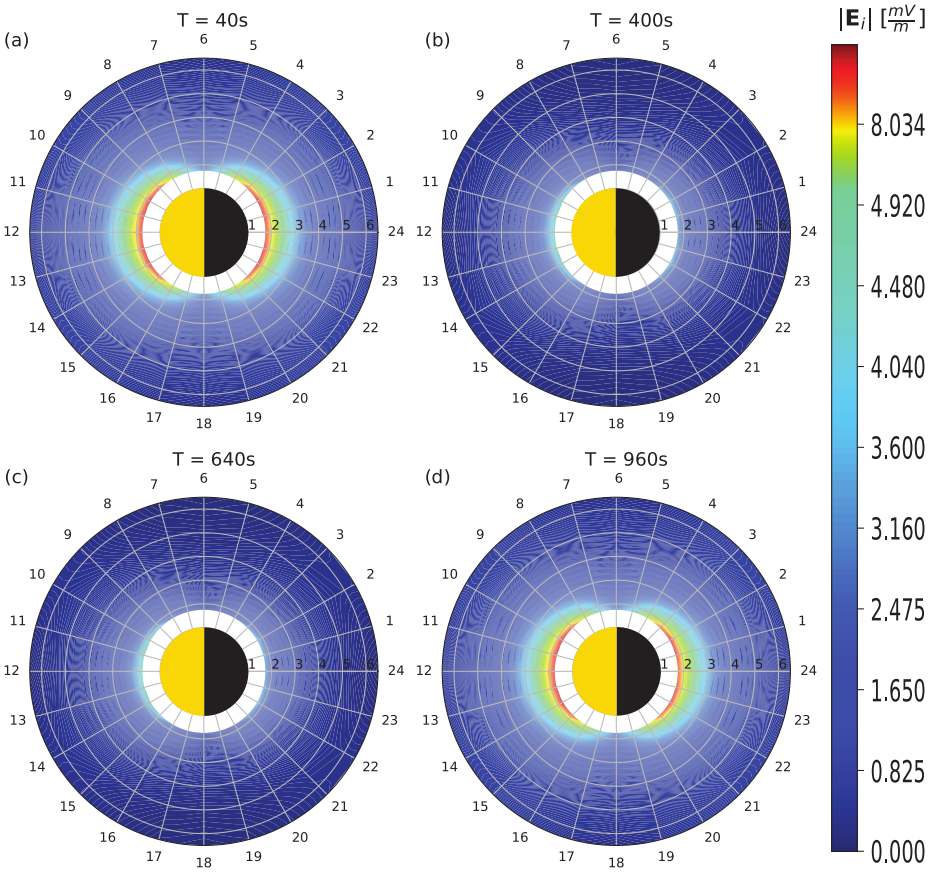

Figure 11. Equatorial $|\mathbf{E}_i|=\sqrt{E^2_{i(x)}+E^2_{i(y)}+E^2_{i(z)}}$ at the four time moments: (a) $t_1 = 40s$, (b) $t_2 = 400s$, (c) $t_3 = 640s$ and (d) $t_4 = 960s$.

tion regarding the changes in drift and associated energy change under the self-consistent inductive electric field will be carried out in the next section.

3 The Effect of Inductive Electric Fields on Drifts, Energy Gain and Pitch angle Change

The inclusion of inductive electric field models, such as the ones discussed in previous section, alters the bounce-averaged coefficients $\left\langle \frac{dR_0}{dt} \right\rangle$, $\left\langle \frac{d\phi_0}{dt} \right\rangle$, $\left\langle \frac{dW}{dt} \right\rangle$ and $\left\langle \frac{d\mu_0}{dt} \right\rangle$ shown in Equations 5, 6, 10 and 11. Previously, the HEIDI model did not account for the effect of inductive electric fields, when calculating the drift coefficients, and consequently, the energization rate and change of pitch-angle did not reflect the dynamics associated with the effect of inductive electric fields. In order to assess how much the inductive electric field affects the dynamics of the ring current ions, we performed and analyzed four

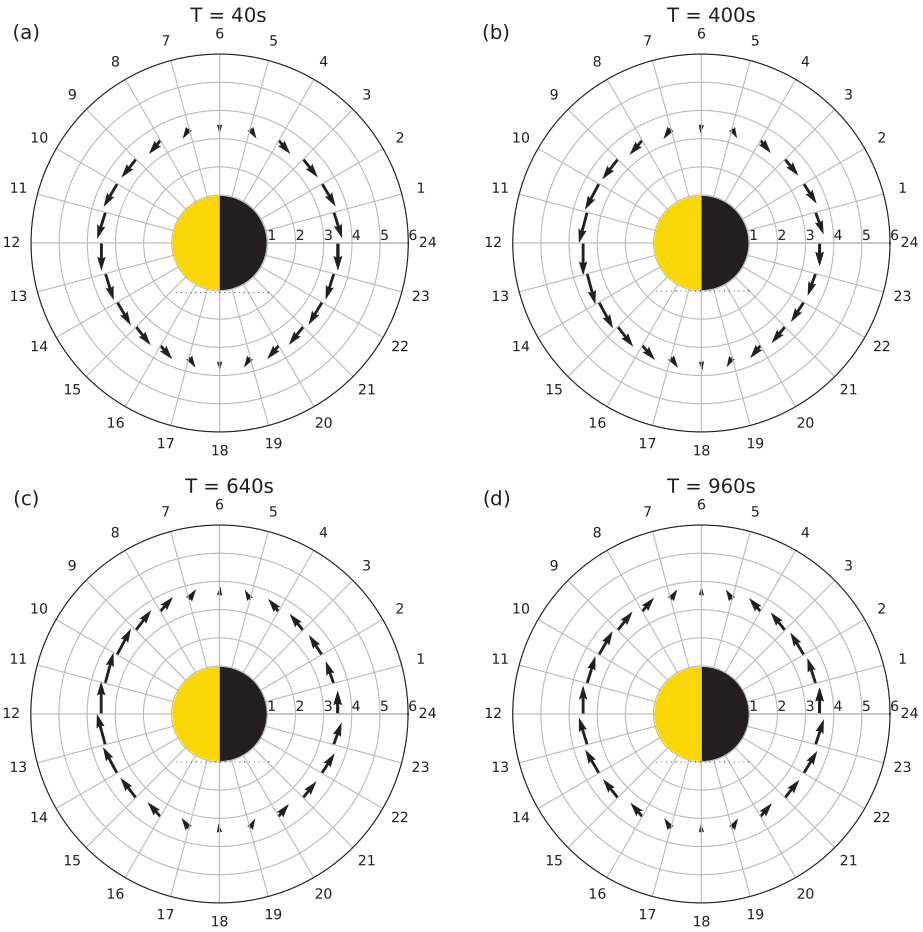

Figure 12. Instantaneous vector $\mathbf{E}_i$ at $3.5R_e$ at the four time moments: (a) $t_1 = 40s$, (b) $t_2 = 400s$, (c) $t_3 = 640s$ and (d) $t_4 = 960s$.

testing cases: two simulation runs that set the magnetic field either as a static dipole or as time dependent field depending on the stretching factor $b(t)$ as expressed in Equation 43. In addition, for each of these simulations, the inductive electric field has been turned on or off. The equatorial bounce-averaged coefficients for the four testing cases over the entire 2000s simulation time, are analyzed and discussed in this section. Meanwhile, we focus our discussion on the results from four different magnetic local time (MLT) sectors at midnight, dawn, noon and dusk (MLT=0,6,12,18), and equatorial radial distance of $3R_E$ away from Earth, with a typical energy of $53.5keV$ and equatorial pitch-angle of 60.5°.

The bounce-averaged total drifts $\left\langle \frac{dR_0}{dt} \right\rangle$ and $\left\langle \frac{d\phi_0}{dt} \right\rangle$ are defined as the superposition of the bounce-averaged magnetic gradient-curvature drift and total equatorial $\mathbf{E}\times$

B drift, as expressed by Equation 5 and 6, where the total equatorial **E**×**B** drift consists of the component contributed by equatorial electrostatic field $\mathbf{E}_{0(\Phi)}$ and inductive field $\mathbf{E}_{0(i)}$. The bounce-averaged magnetic gradient-curvature drift $\langle \mathbf{v}_{GC} \rangle$ is calculated from the instantaneous magnetic field configuration based on Equation 7, the **E**×**B** is defined using the electrostatic field based on the electrostatic potential from the Weimer model (Weimer, 1996), which is dependent on input storm Kp index, and the inductive field calculated from the instant local inductive electric field and magnetic field topology. The local rate of change of energy $\left\langle \frac{dW}{dt} \right\rangle$ and pitch-angle $\left\langle \frac{d\mu_0}{dt} \right\rangle$ (which follow 10 and 11, respectively) have explicit dependence on local total drifts $\left\langle \frac{dR_0}{dt} \right\rangle$ and $\left\langle \frac{d\phi_0}{dt} \right\rangle$, consequently the change of total drifts also results in change of energy and pitch-angle rate of change. All ion drift components, in addition to the resulting bounce-averaged total drift, energization rate and pitch-angle rate of change at certain locations (with each of the three inductive electric models) are discussed in this section. To avoid confusion and ambiguity, for all the figures in this section we specify the symbols of drift velocity components to be: $\langle V(GC) \rangle$ denotes the equatorial bounce-averaged magnetic gradient-curvature drift, $V(inductive)$ represents the equatorial **E**×**B** drift resulted from a specific inductive electric field, and $V(\Phi)$ represents the equatorial $\mathbf{E} \times \mathbf{B}$ drift derived via electrostatic potential field, such as the one constructed from the input Kp-dependent Weimer model. Furthermore, to help organizing and interpreting the results in each figure, we employ the following plotting convention: The dash line style represents the case of static dipole magnetic field; the solid line style represents the case of time dependent magnetic field following the stretching factor as in 43. Different MLTs with the inductive electric field model turned or off are represented by different color combinations specified by the legends.

Please notice that the local radial magnetic gradient-curvature drift $\langle V_r(GC) \rangle$ at the four MLTs (midnight, dawn, noon and dusk) is a trivial drift component, even though the magnetic field becomes non-dipolar, by coincidence. This has been mathematically verified, by substituting the magnetic field expressions in Equation 13, 14 and 15 into $\mathbf{v}_{GC}$ expression 7, and confirmed that the radial magnetic gradient-curvature drift is vanishing at dawn, dusk, midnight and noon regardless of the field stretching. On the other hand, at locations other than dawn, dusk, midnight and noon, the radial magnetic gradient-curvature drift is non-trivial if the magnetic field is stretched away from dipole. The azimuthal magnetic gradient-curvature drift is always non-zero at all MLTs.

3.1 MLT Dependent Inductive Electric Field

The MLT dependent inductive electric field discussed in Section 2.3.1 and illustrated in Figure 3, which is exactly zero at noon and midnight (therefore not contributing to local drift, energy change, and pitch-angle change at these MLTs), peaks at dawn (where it points from dusk to dawn) and dusk (where it points from dawn to dusk). Consequently, the local total drifts at midnight and noon are not affected by the MLT dependent electric field setup. Figure 13 shows the non-trivial local drift velocity components, energy change and pitch-angle change at midnight (MLT=0) and noon (MLT=12). The local inductive drift $V(inductive)$ at both midnight and noon are zero all the time (due to the vanishing local inductive electric field, by setup), therefore not being included in Figure 13, and so is the radial component of magnetic gradient-curvature drift $\langle V_r(GC)\rangle$, as explained earlier. Therefore, the MLT dependent inductive electric field has no effect on local drift kinetic solution at midnight and noon: turning on and turning off the inductive electric field model produces the same local result at both midnight and noon, regardless of the magnetic field being time-dependent or not, hence the blue and red $\left\langle \frac{dR_0}{dt} \right\rangle$, $\left\langle \frac{d\phi_0}{dt} \right\rangle$, $\left\langle \frac{dW}{dt} \right\rangle$ and $\left\langle \frac{d\mu_0}{dt} \right\rangle$ curves overlaps the black and green, as reflected in panel (d), (e), (f) and (g), respectively, of Figure 13.

Furthermore, at midnight and noon we see strong azimuthal (westward) magnetic gradient-curvature drift $\langle V_\phi(GC)\rangle$ of the order of several km/s, as reflected in panel (a) of Figure 13, while weak azimuthal electrostatic potential drift $V_\phi(\Phi)$ reflected in panel (c), which is in the order of tens of m/s. Hence, the local total azimuthal drift $\left\langle \frac{d\phi_0}{dt} \right\rangle$ at midnight and noon is dominated by the azimuthal component of magnetic gradient-curvature drift $\langle V_\phi(GC)\rangle$, as reflected in panel (e). In turn, the total local radial drift $\left\langle \frac{dR_0}{dt} \right\rangle$ at midnight and noon is dominated by the electrostatic potential drift $V_r(\Phi)$ (which is reflected in panel (d)). In addition, comparing the speed of total azimuthal drift $\left\langle \frac{d\phi_0}{dt} \right\rangle$ in panel (e) with the speed of total radial drift $\left\langle \frac{dR_0}{dt} \right\rangle$ in panel (d), one finds that the local azimuthal drift is much faster than the local radial drift (in the order of tens of m/s), which means that the ring current ion species placed around midnight and noon drifts westward without penetrating much into lower L shells.

During the stretching stage ($0 \leq t \leq 500s$ and $1000s \leq t \leq 1500s$), the local magnetic field is intensified on dayside and weakened on nightside, which results in a decelerating azimuthal (westward) drift at noon (Figure 13 panel (a) and (e), red curves)

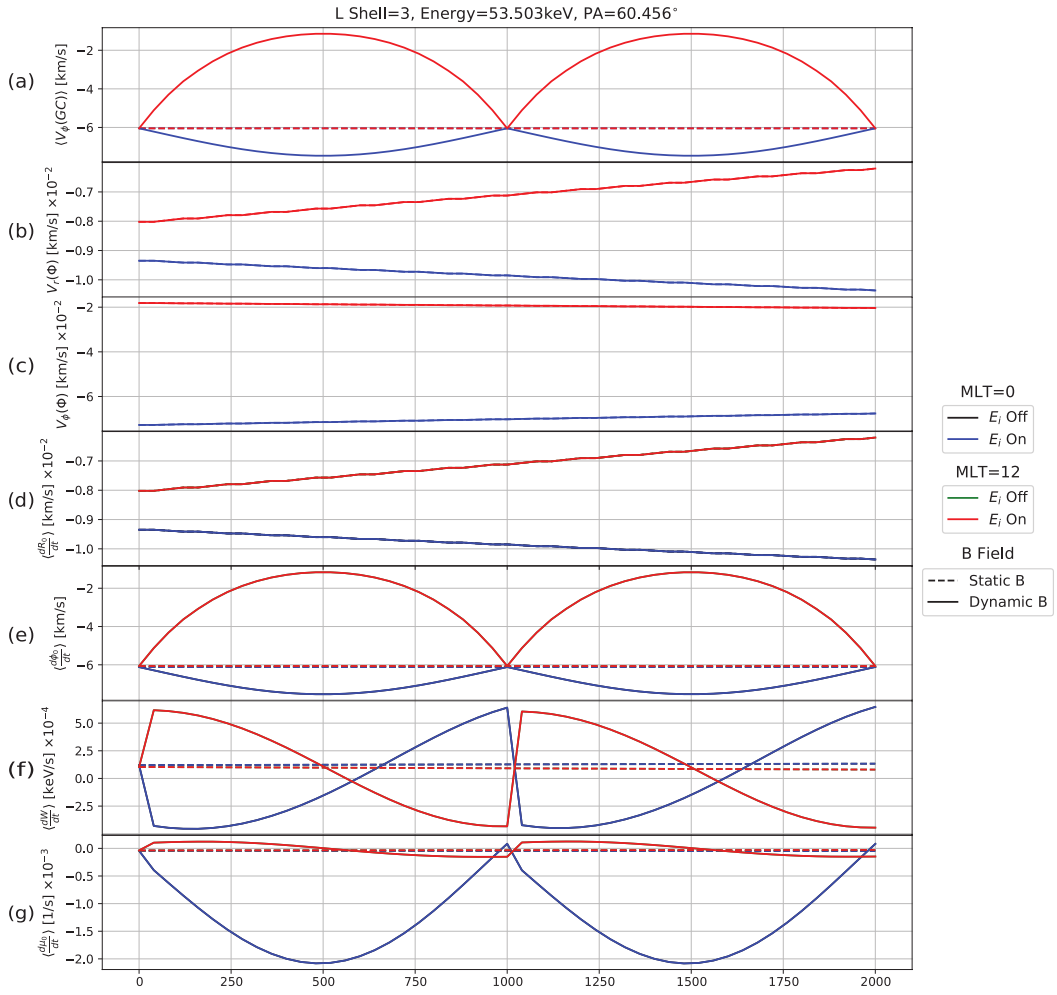

Figure 13. Equatorial drift components, energization rate $\left\langle \frac{dW}{dt} \right\rangle$ and pitch-angle change $\left\langle \frac{d\mu_0}{dt} \right\rangle$ at MLT=0 (midnight) and MLT=12 (noon), with the MLT dependent inductive electric field model described in Section 2.3.1. The black and green curves represent the local results at midnight and noon, respectively, with inductive electric field model turned off; the blue and red curves represent the local results at midnight and noon, respectively, with inductive electric field model turned on.

while accelerating azimuthal (westward) drift at midnight (Figure 13 panel (a) and (e), blue curves), and the reverse is true during the dipolarization stage ($500s \leq t \leq 1000s$ and $1500s \leq t \leq 2000s$). In general, as the magnetic field is stretched away from the dipole configuration, the ion azimuthal (westward) magnetic gradient-curvature drift velocity $\langle V_\phi(GC) \rangle$ decreases from nightside to dayside (which is reflected in Figure 13 panel (a) solid blue and red curves, as an extreme example at midnight and noon) due to the

changing magnetic gradient-curvature. The local equatorial azimuthal magnetic gradient-curvature drift at a certain radial distance, under dipole magnetic field configuration, is the same for all MLTs, so the dashed red curve in panel (a) overlaps with all dashed curves in other colors. Comparing the extent of change of local magnetic gradient-curvature drift at midnight and noon with respect to the static dipolar magnetic field case (solid blue and red curves, with respect to dashed red line, in panel (a)), one finds that local azimuthal magnetic gradient-curvature drift at noon experience much greater deviation from dipole case, compared with the one at midnight. This corresponds to the property of our magnetic field setup, that with the same magnetic stretching factor $b(t)$, the change of local magnetic field on dayside is greater than the change on nightside (away from the dipole field), as discussed in Methodology section.

Moreover, because the $\mathbf{E}\times\mathbf{B}$ velocity is proportional to $\frac{1}{B}$, where B denotes the local magnetic field intensity, stronger magnetic field tends to decelerate the local $\mathbf{E}\times\mathbf{B}$ drift. Hence, the magnetic cavity can act as a magnetic barrier: as ions drift westward from midnight toward dusk under the stretched magnetic field configuration, they get decelerated and consequently start to pile up in the evening sector (18MLT — 0MLT quadrant), increasing the total local ion pressure; in the postdawn sector (0MLT — 6MLT quadrant), ions are accelerated as they drift from dawn to midnight, therefore reducing the total ion density and pressure. This matches with the evolution of energetic ions distribution around the main phase of certain storm studied by Ilie et al. (2012); Nishimura, Shinbori, Ono, Iizima, and Kumamoto (2007); V. A. Sergeev et al. (1998). As the magnetic field is being stretched on the dayside, local magnetic field at noon increases, therefore adiabatically energizes ring current ion species, and the opposite is true at nightside (panel (f), red and blue curves, respectively). This agrees with the observation that particles convected Earthward from weak magnetic field to stronger magnetic field regions are adiabatically energized and contribute to the ring current hot ion populations. Furthermore, the changing magnetic field also alters the bounce path length and magnetic mirror points along each field line (except at dawn and dusk, where it remains dipolar), consequently affecting the equatorial pitch-angle of ion species with certain initial equatorial pitch-angle. The local equatorial pitch-angle rate of change at noon and midnight possesses opposite trend as the magnetic field changes with time, as illustrated with the $\left\langle \frac{d\mu_0)}{dt} \right\rangle$ curves in panel (g), agreeing with the fact that the magnetic field on the dayside and nightside changes in the opposite way, in time.

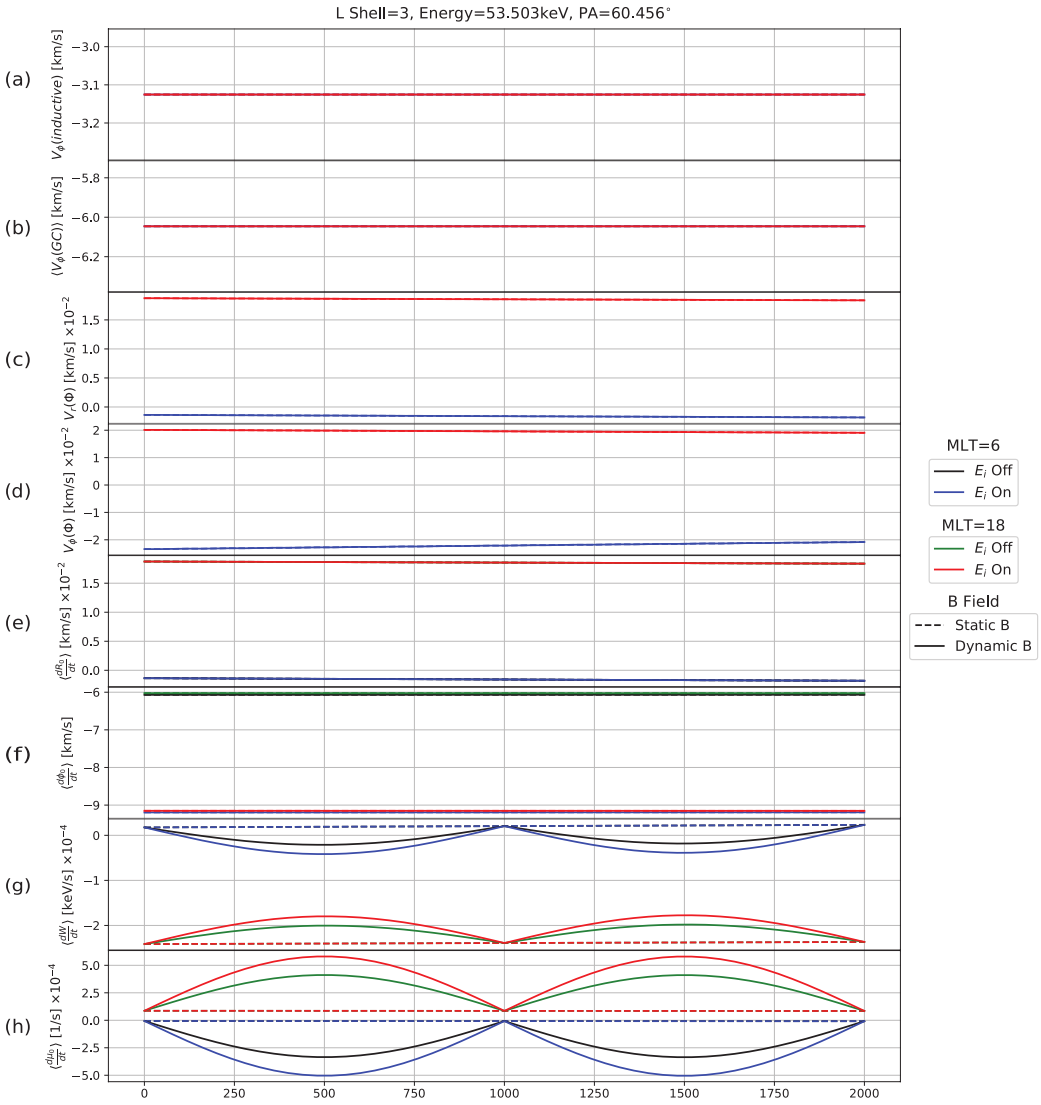

Figure 14. Equatorial drift components, energization rate $\left\langle \frac{dW}{dt} \right\rangle$ and pitch-angle change $\left\langle \frac{d\mu_0}{dt} \right\rangle$ at MLT=6 (dawn) and MLT=18 (dusk), with the MLT dependent inductive electric field model described in Section 2.3.1. The black and green curves represent the local results at dawn and dusk, respectively, with inductive electric field model turned off; the blue and red curves represent the local results at dawn and dusk, respectively, with inductive electric field model turned on.

Figure 14 shows the non-trivial local drift velocity components, energy change and pitch-angle change at dawn (MLT=6) and dusk (MLT=18), where the MLT dependent electric field reaches the peak value, but only contributes to the azimuthal drift (local radial inductive drift $V_r(inductive)$ at dawn and dusk is trivial drift component, due to

598 the inductive electric field setup, so not included in Figure 14). Imposing such MLT de-
599 pendent electric field essentially accelerates the westward drift everywhere on the equa-
600 torial plane, except at midnight and noon (where the MLT dependent electric field is zero).
601 The azimuthal inductive drift $V_\phi(inductive)$ at dawn and dusk possesses equal magni-
602 tude and direction (westward), and the local magnetic field at dawn and dusk stays dipo-
603 lar regardless of the stretching, thus the red curve overlaps with the other colors, as showed
604 in Figure 14 panel (a). Panel (f) shows that significant change in the local total azimuthal
605 drift $\left\langle \frac{d\phi_0}{dt} \right\rangle$ at dawn and dusk has been resulted from such imposed MLT dependent elec-
606 tric field, as we can clearly distinguish that the blue curve goes below the black, and the
607 red curve goes below the green, meaning that the inductive electric field acts to increase
608 the westward drift. The azimuthal magnetic gradient-curvature drift $\langle V_\phi(GC) \rangle$ at dawn
609 and dusk are equal and not changing with time even if the magnetic field is changing from
610 dipole, therefore the red curves again overlaps with the other colors in panel (b). Fur-
611 thermore, just like at midnight and noon, the radial magnetic gradient-curvature drift
612 $\langle V_r(GC) \rangle$ at dawn and dusk is still trivial, therefore not included in Figure 14. The to-
613 tal radial drift $\left\langle \frac{dR_0}{dt} \right\rangle$ at dawn and dusk is dominated by the electrostatic potential drift
614 $V_r(\Phi)$, while both inductive drift $V_\phi(inductive)$ and magnetic gradient-curvature drift
615 $\langle V_\phi(GC) \rangle$ contribute to the total azimuthal drift $\left\langle \frac{d\phi_0}{dt} \right\rangle$.

616 Although the local magnetic field at dawn and dusk stays dipolar regardless of the
617 stretching, the energization rate $\left\langle \frac{dW}{dt} \right\rangle$ changes after including the inductive electric field,
618 since the total azimuthal drift $\left\langle \frac{d\phi_0}{dt} \right\rangle$ is altered. At dawn, the MLT dependent electric
619 field serves to deplete the energy of ions (as the blue curve is below the black in panel
620 (g)), while at dusk it energizes them (as the solid red curve is above the green and in panel
621 (g)). Please note that because the local magnetic field at dawn and dusk is always dipo-
622 lar, allowing the magnetic field stretch with time or not does not make a difference on
623 the local rate of change of energy $\left\langle \frac{dW}{dt} \right\rangle$ and pitch-angle $\left\langle \frac{d\mu_0}{dt} \right\rangle$ (under the case that the
624 inductive electric field is turned off), hence in panel (g) and (h), the dashed blue curve
625 overlaps with the dashed black curve and the dashed red curve overlaps with the dashed
626 green curve.

627 ### 3.2 Propagating Gaussian Pulse Inductive Electric Field

628 The propagating Gaussian pulse electric field discussed in Section 2.3.2 is set to start
629 at $5R_E$ at $t = 0$, and passes through $L = 3$ around $t = 1333.33s$, as showed in Figure

4. The pulse peak is centered at midnight, and decreases exponentially in the azimuthal direction. It is polarized only in azimuthal direction, implying that the resulting azimuthal inductive drift $V_\phi(inductive)$ is zero, and radial inductive drift $V_r(inductive)$ points Earthward.

The solution for the equatorial drift components, energization rate $\left\langle \frac{dW}{dt} \right\rangle$, and pitch-angle change $\left\langle \frac{d\mu_0}{dt} \right\rangle$, again, are extracted at a radial distance of $3R_E$ on the nightside, and presented in Figure15. It can be seen that the transient inductive electric serves as an intensive local accelerator, associated with notable radial Earthward transport, as illustrated by the pulse shape of blue curves in Figure 15 panel (a), which shows the evolution of local radial inductive drift at midnight. Such a rapid and intense Earthward propagating pulse implies that energetic ring current ions can penetrate into lower L shells, within a short period of time. The difference between the dashed and solid blue curves in panel (a) is due to the weakening of local magnetic field at midnight as the field is stretched away from dipole configuration, and we observe that the stretching of magnetic field serves to further transport ions Earthward on nightside, due to the weakening in the local magnetic field that enhances $\mathbf{E} \times \mathbf{B}$ drift. The azimuthal inductive drift $V_\phi(inductive)$ is the trivial drift component, hence not showed in Figure 15. The total radial drift $\left\langle \frac{dR_0}{dt} \right\rangle$ at midnight is dominated by the radial inductive drift $V_r(inductive)$ triggered by the pulse, as reflected by its pulse shape of dashed and solid blue curves in Figure 15 panel (e), while the total azimuthal drift is dominated by the magnetic gradient-curvature drift $\langle V_\phi(GC) \rangle$, as reflected in panel (f). Furthermore, the pulse inductive electric field has notable effect on local energization at the time when the pulse passes through the measurement location at $3R_E$, as reflected by the sharp increase of midnight $\left\langle \frac{dW}{dt} \right\rangle$ represented by dashed and solid blue curves in panel (g), which has magnitude around several tens of keV/s and lasts for around 200s. This suggests that the transient pulse electric field has the potential to rapidly and effectively energize the particles from low energy to high energy in a short time interval and spatial distance, supporting the observations that ions with initial energy of tens of keV can be accelerated up to hundreds of keV on nightside during substorms.

The magnitude of pulse electric field exponentially decreases away from midnight in the azimuthal direction, and the effect of the pulse electric field also weakens, until it becomes negligible at noon. As a result, turning the pulse electric field on and off does not notably affect the local particle drifts and energization rates at noon, which can be

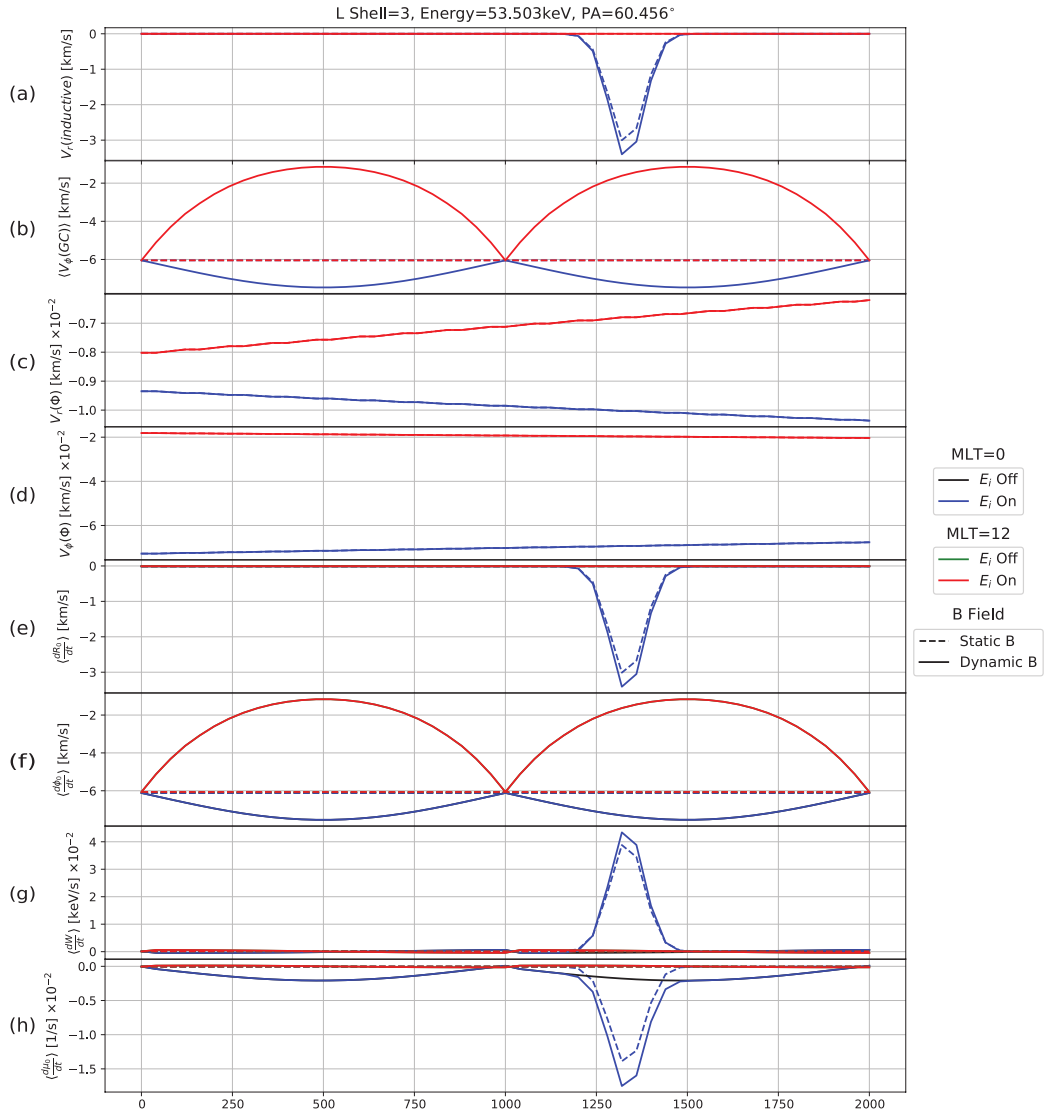

Figure 15. Equatorial drift components, energization rate $\left\langle \frac{dW}{dt} \right\rangle$ and pitch-angle change $\left\langle \frac{d\mu_0}{dt} \right\rangle$ at MLT=0 (midnight) and MLT=12 (noon), with the propagating pulse inductive electric field model described in Section 2.3.2. The black and green curves represent the local results at midnight and noon, respectively, with inductive electric field model turned off; the blue and red curves represent the local results at midnight and noon, respectively, with inductive electric field model turned on.

confirmed by observing that the red curve overlaps with the green in Figure 15 panel (e), (f), (g) and (h). In turn, at dawn and dusk, the radial total drift $\left\langle \frac{dR_0}{dt} \right\rangle$ and energization rate $\left\langle \frac{dW}{dt} \right\rangle$, represented by Figure 16 panel (e) and (g), have the same pattern with the ones at midnight, with $\left\langle \frac{dR_0}{dt} \right\rangle$ dominated by $V_r(inductive)$ triggered by the pulse elec-

667 tric field, except that the peak magnitude (for both the drift and energization rate) is
668 around ten times smaller than the one at midnight, due to the weakening of the mag-
nitude of pulse.

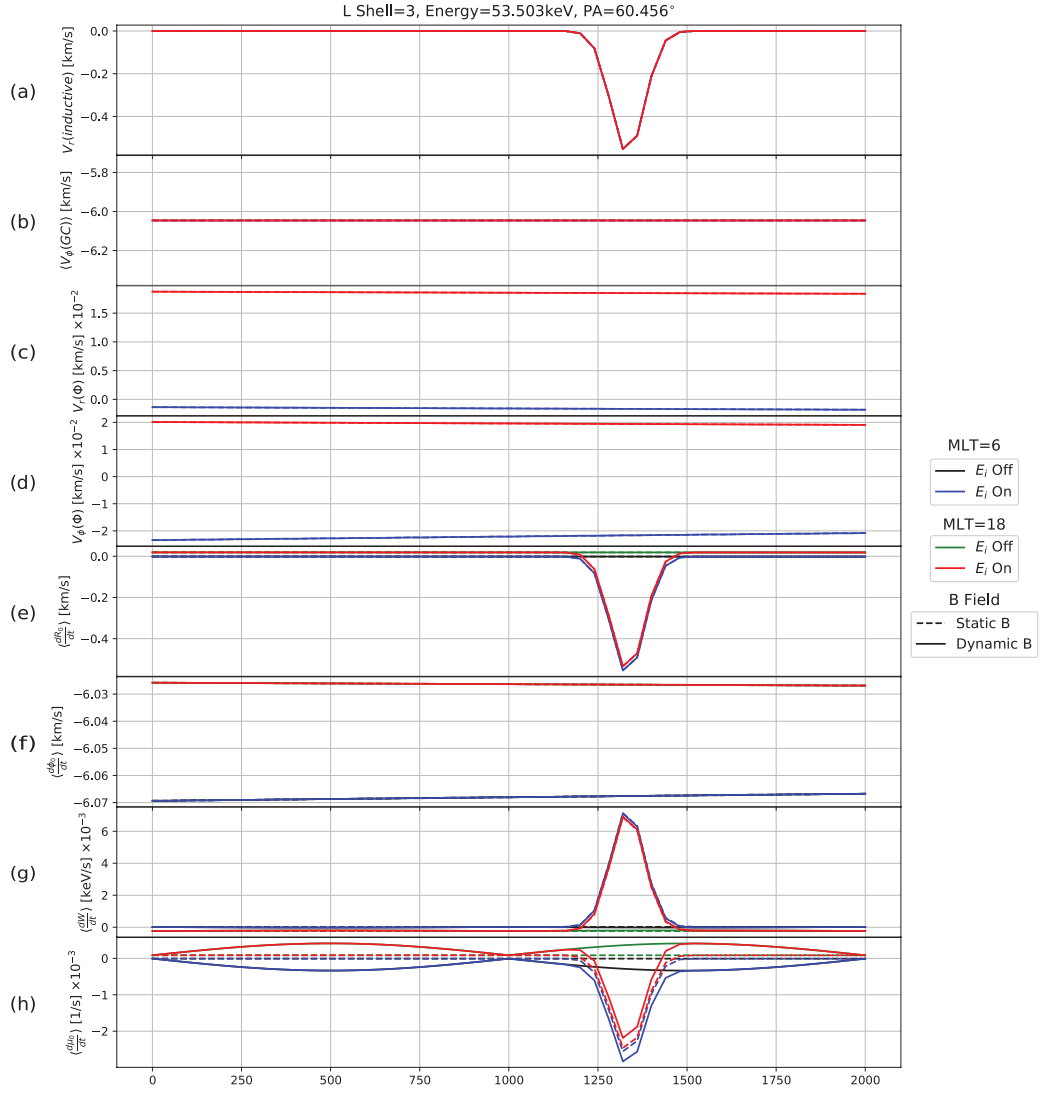

Figure 16. Equatorial drifts, energization rate $\left\langle \frac{dW}{dt} \right\rangle$ and pitch-angle change $\left\langle \frac{d\mu_0}{dt} \right\rangle$ at MLT=6 (dawn) and MLT=18 (dusk), with the propagating pulse inductive electric field model described in Section 2.3.2. The black and green curves represent the local results at dawn and dusk, respectively, with inductive electric field model turned off; the blue and red curves represent the local results at dawn and dusk, respectively, with inductive electric field model turned on.

669

3.3 Self-Consistent Inductive Electric Field

The self-consistent inductive electric field is calculated from the temporal change of magnetic field $\frac{\partial \mathbf{B}}{\partial t}$ based on Faraday's law, as described in Section 2.3.4. During the stretching phase ($0 \leq t \leq 500s$ or $1000s \leq t \leq 1500s$), the self-consistent electric field points from dawn toward dusk, and reverses as the magnetic field recovers ($500 \leq t \leq 1000s$ or $1500s \leq t \leq 2000s$), as illustrated in Figure 12. Similar with the direction of the Gaussian pulse electric field, the self-consistent inductive electric field is mostly azimuthal, meaning that it injects or expels plasma radially across L shells, but does not affect the azimuthal component of the overall drift significantly. A strong inductive electric field is located around midnight and noon, where the local temporal magnetic field change is large, resulting in a strong radial inductive drift $V_r(inductive)$ at midnight and noon, as reflected by the red and blue curves in Figure 17 panel (a). More specifically, we observe strong inward radial inductive drift triggered by the inductive electric field on nightside while outward radial inductive drift on dayside, as the magnetic field being stretched, and the reverse is true when the magnetic field dipolarizes. Therefore, at midnight and noon, the local total radial drift $\left\langle \frac{dR_0}{dt} \right\rangle$ is dominated by the radial inductive drift $V_r(inductive)$, and the local total azimuthal drift $\left\langle \frac{d\phi_0}{dt} \right\rangle$ is dominated by the azimuthal magnetic gradient-curvature drift $\langle V_\phi(GC) \rangle$, as showed in Figure 17 panel (e) and (f). As ions are being injected Earthward on the nightside, they are continuously energized, with a significant energization rate up to several tens of keV/s (as reflected in panel (g)). The reverse is true for ions on dayside, that are losing energy as drifting from stronger magnetic field to weaker magnetic field (away from the Earth). Such a trend represents a notable injection of energetic ions from plasma sheet into inner magnetospheric ring current region (hence accumulating local energy) on nightside, and an energy loss on the dayside, as charged particles are being decelerated due to the intensification of the dayside magnetic field, which acts as a magnetic barrier.

At dawn and dusk, the self-consistent inductive electric field becomes negligible compared with the one at midnight and noon, so does the local effect of inductive electric field on drift components, energization, and pitch angle change. However, we still observe weak azimuthal inductive drift $V_\phi(inductive)$ at dawn and dusk, as showed in Figure 18 panel (a), due to the presence of a weak local inductive electric field at these locations. In addition, the azimuthal inductive drift $V_\phi(inductive)$, which magnitude is only up to several $10^{-4} km/s$, is negligible compared with the local azimuthal magnetic gra-

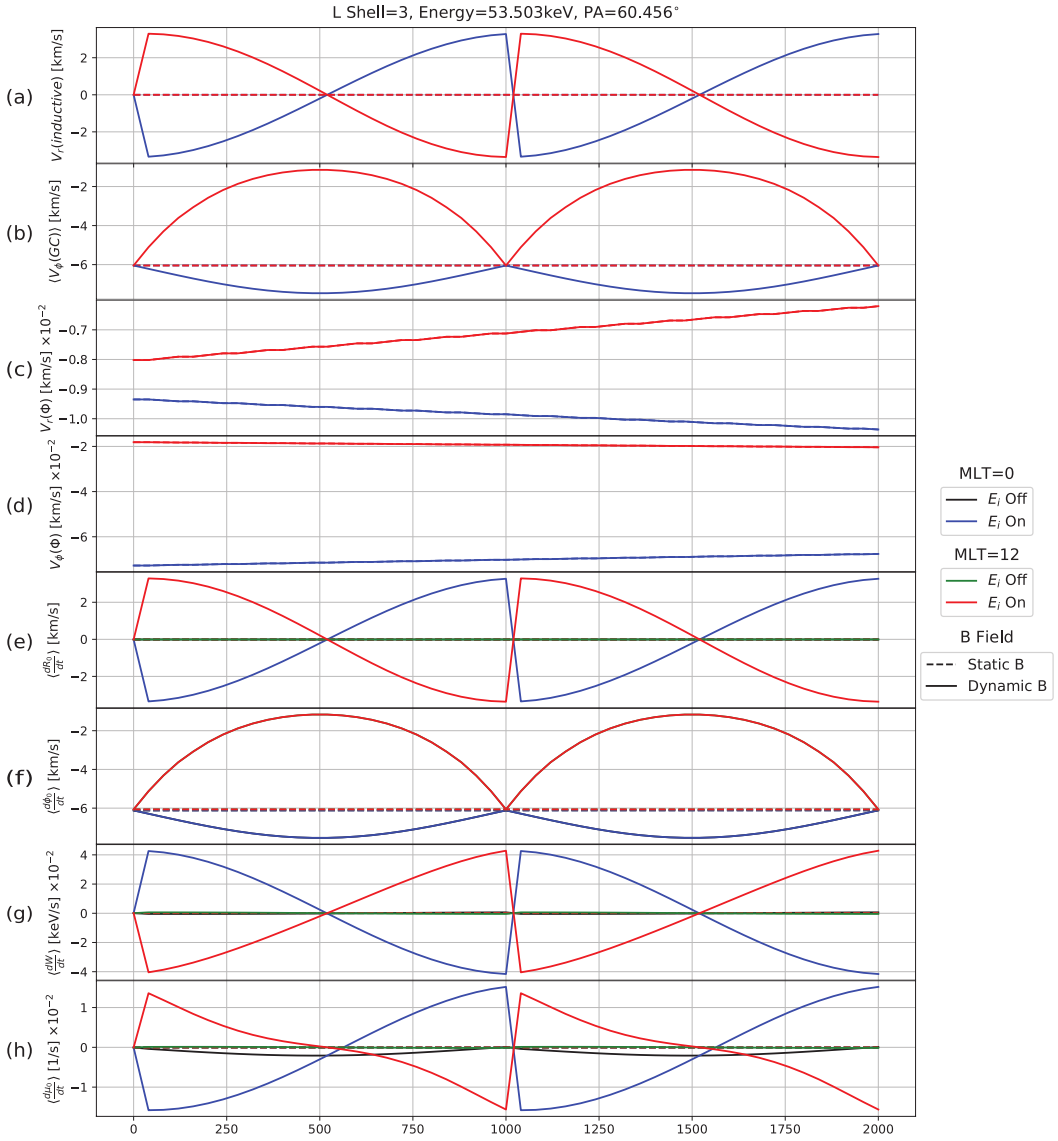

Figure 17. Equatorial drift components, energization rate $\left\langle \frac{dW}{dt} \right\rangle$ and pitch-angle change $\left\langle \frac{d\mu_0}{dt} \right\rangle$ at MLT=0 (midnight) and MLT=12 (noon), with the self-consistent inductive electric field model described in Sections 2.3.4 and 2.3.6. The black and green curves represent the local results at midnight and noon, respectively, with inductive electric field model turned off; the blue and red curves represent the local results at midnight and noon, respectively, with inductive electric field model turned on.

dient curvature drift $\langle V_\phi(GC) \rangle$, which magnitude is several km/s as showed in panel (b). As a result, the total local radial drift $\left\langle \frac{dR_0}{dt} \right\rangle$ at dawn and dusk is dominated by the radial electrostatic potential drift $V_\phi(\Phi)$, and the total local azimuthal drift $\left\langle \frac{d\phi_)}{dt} \right\rangle$ is dominated by the azimuthal magnetic gradient-curvature drift $\langle V_\phi(GC) \rangle$, as reflected in Fig-

ure 18 panel (e) and (f). Correspondingly, the local energization rate $\left\langle \frac{dW}{dt} \right\rangle$ at dawn and dusk, whose magnitude is in the order of $10^{-4} keV/s$ as showed in panel (g), is also negligible compared with the $\left\langle \frac{dW}{dt} \right\rangle$ at midnight and noon, where the inductive electric field is strong.

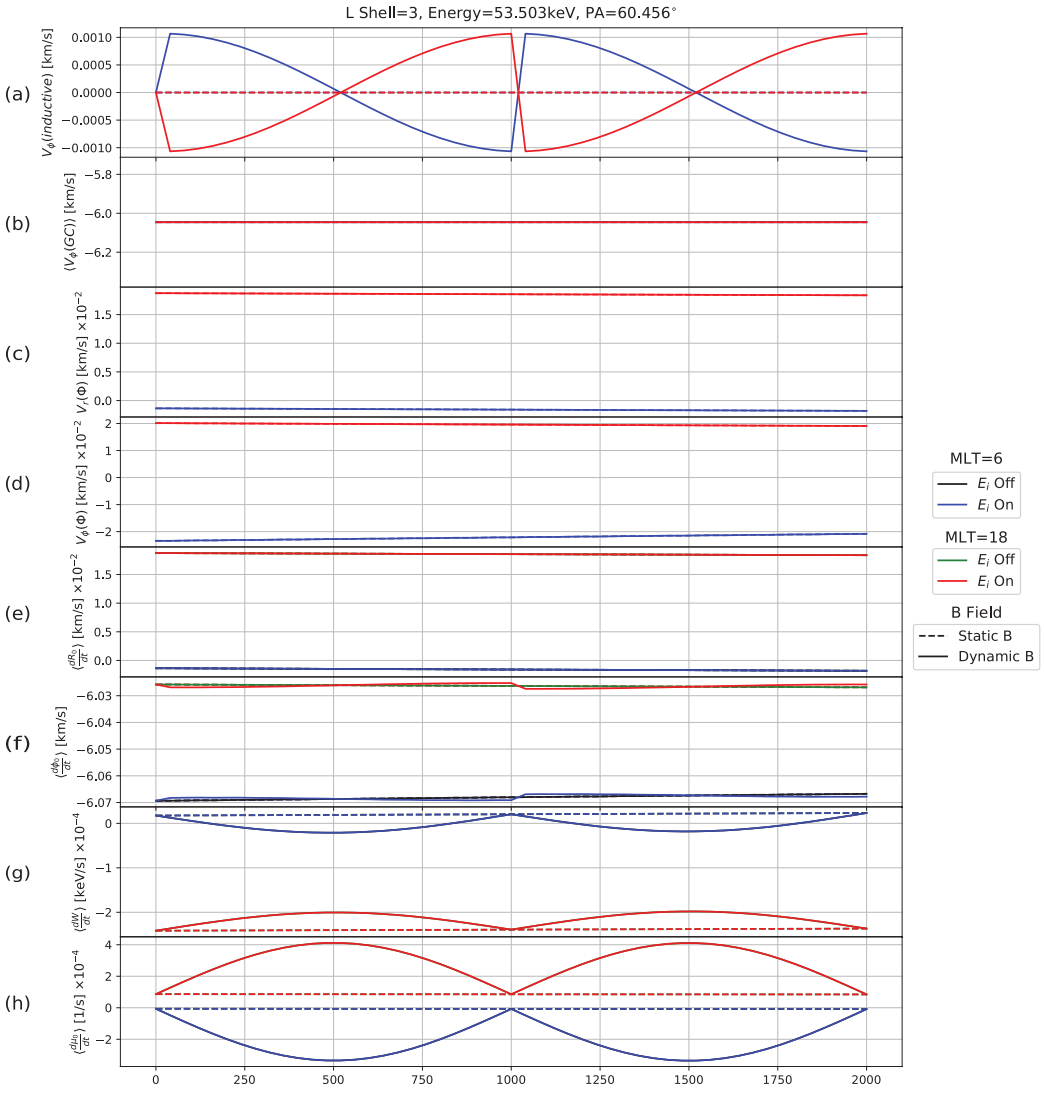

Figure 18. Equatorial drifts, energization rate $\left\langle \frac{dW}{dt} \right\rangle$ and pitch-angle change $\left\langle \frac{d\mu_0}{dt} \right\rangle$ at MLT=6 (dawn) and MLT=18 (dusk), with the self-consistent inductive electric field model described in Sections 2.3.4 and 2.3.6. The black and green curves represent the local results at dawn and dusk, respectively, with inductive electric field model turned off; the blue and red curves represent the local results at dawn and dusk, respectively, with inductive electric field model turned on.

The self-consistent inductive electric field associated with such intensively stretching and dipolarization process as expressed in Equation 43 has significant effect on the global evolution of the ring current. Figure 19 column (a) shows the relative equatorial total ion pressure change from the simulation that assumes a static dipole magnetic field and zero inductive electric field, to a simulation that allows a changing magnetic field and zero inductive electric field. Column (b) shows the relative equatorial total ion pressure change from a simulation that assumes a static dipole magnetic field and zero inductive electric field, to a simulation that allows a changing magnetic field and associated self-consistent inductive electric field. Note that for all simulations, particles (as sources) were injected from the geosynchronous orbit on nightside (the outer equatorial simulation domain boundary at 6.5 R_E) every 40s, and H^+, He^+ and O^+ are the ring current ions considered for the total pressure plot.

From Figure 19 column (a), we note that the stretching magnetic field (without considering the associated inductive electric field) increases the buildup of ring current ions in the evening sector and depletes the ion pressure in the morning sector (6MLT — 12MLT quadrant). This is because the stretching of magnetic field notably changes the magnetic gradient-curvature drifts, increasing the drift speeds on nightside (weakening magnetic field regions) while decreasing the drift speeds on dayside (enhanced magnetic field regions). Midnight and noon experiences the largest changes in the local magnetic gradient-curvature drifts, while the local drifts at dawn and dusk remain unchanged. By contrast, the dipole magnetic field produces zero radial magnetic gradient-curvature drift and uniform azimuthal (westward for ions) magnetic gradient-curvature drift at a fixed radial distance from the Earth on the magnetic equatorial plane. This pulls ions faster from noon to dawn in westward direction, causing the depletion of ions in the morning sector (therefore decreasing ion pressure), and pushes ions slower from midnight to dusk in westward direction, resulting in the accumulation of ions in the evening sector. In addition, the injected particles neither drift to noon nor penetrate deeper into lower L shells on dayside. This is due to the significant slow down of magnetic gradient-curvature drift on dayside, as the magnetic field is stretched. Note that these changes are also due in part to the change in the field line length contained in the $\frac{\partial I}{\partial t}$, and the explicit time dependence $\frac{\partial B_0}{\partial t}$ of energy and pitch angle change in Equations 10 and 11. Column (b) shows the effect of self-consistent inductive electric field associated with the stretching of magnetic field. During the stretching phase ($0 \leq t \leq 500s$), the effect of the self-consistent

inductive electric field is to provide an additional means of acceleration, allowing nightside charged particles access to the lower L shells, while particles drifting on the dayside are pushed toward the magnetopause, toward weaker magnetic field regions. This allows for an accumulation of ion pressure on nightside, while depleting it on dayside, as it can be seen at $T = 40s$ and $T = 400s$. During the dipolarization phase ($0 \leq t \leq 500s$), the self-consistent inductive electric field acts to pull ions Earthward on dayside while pushing them away on nightside, therefore accumulating ion pressure on dayside and depleting ion pressure on nightside. As a result, we observe notably reduced ion pressure on nightside and an increase in ion pressure on dayside, at the end of dipolarization phase ($T = 960s$), compared with the end of stretching phase ($T = 400s$). The magnetic field intensification on dayside always act as a barrier to the drift and transport of ring current ion species, and produces notable asymmetry of ring current total ion pressure around the dawn — dusk meridian. This effect is reflected in the factor of two difference in the overall particle pressure, as the self-consistent inductive electric field is accounted for. The presence of a self-consistent inductive electric field alters the overall particle trajectories, energization and pitch angle, resulting in significant changes in the topology and strength of the ring current. Therefore, not taking the effect of inductive electric field (even if including the changes of magnetic gradient-curvature drift) into account leads to a mis-estimation on the kinematics of ring current ion species, and the associated ring current evolution over time.

4 Discussion and Conclusion

Kinetic models are of crucial importance in the study of inner magnetosphere ring current dynamics. The HEIDI model (Ilie et al., 2012; Liemohn et al., 2004) is an inner magnetospheric kinetic drift model that solves the time-dependent and bounce-averaged Boltzmann equation for the equatorial phase space distribution function of ring current ion species. In this paper we present an important improvement to HEIDI: new drift terms associated with the inductive electric field are incorporated into the calculation of bounce-averaged coefficients for the equatorial phase-space distribution function, and the effects of inductive drifts on the total drift and energization rate are tested under certain inductive electric field models for the first time. This new version of the HEIDI model is capable of accounting for the inductive component of electric field based on various (empirically or self-consistently defined) models. The effects of the distorted magnetic field

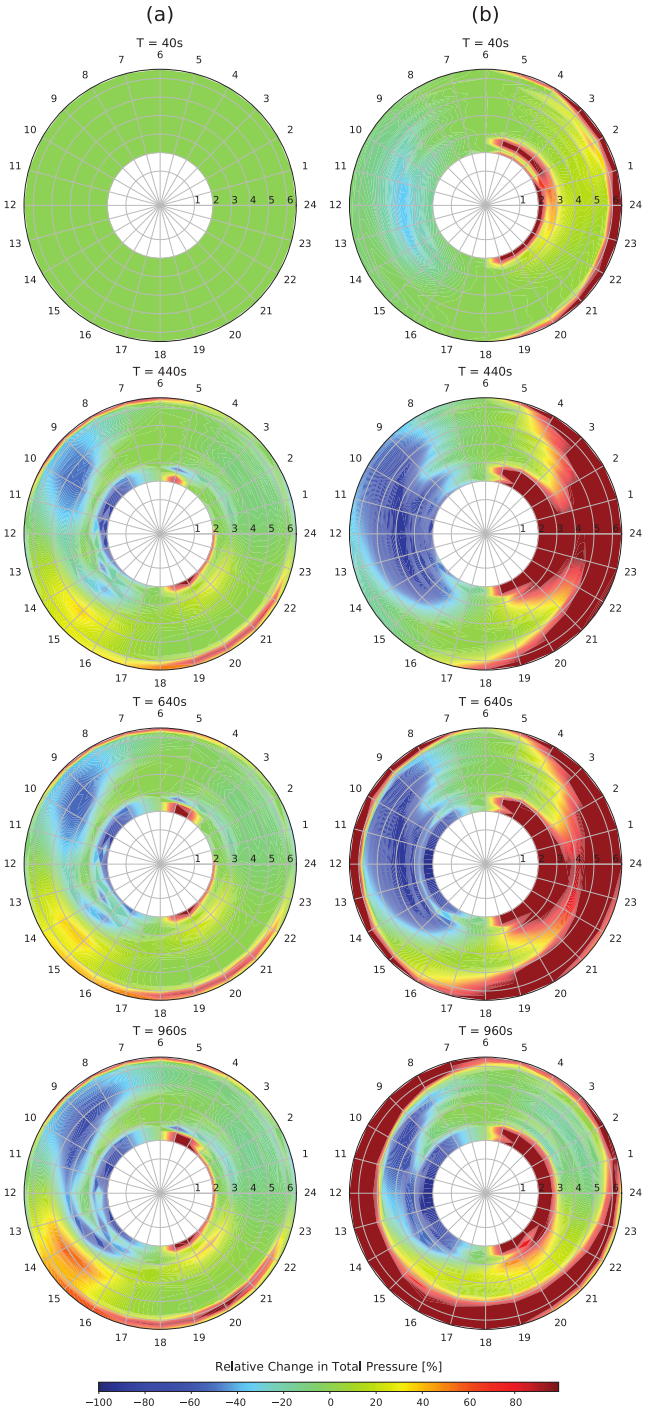

Figure 19. Relative equatorial total ion pressure change at the four time moments, from the case of static dipole magnetic field and zero inductive electric field setup, to column (a): the case of changing magnetic field plus zero inductive electric field setup, and column (b): the case of changing magnetic field plus associated self-consistent inductive electric field setup.

on ring current ion species are investigated first, and we showed that the local change in particles' energy and pitch-angle under distorted magnetic field deviate significantly away from the ones under dipole magnetic field. Moreover, the distorted magnetic field configuration breaks down the symmetry of magnetic gradient-curvature drift in dipole case, accelerating charged particles on the nightside and decelerating them significantly on dayside. Such a change on drift velocity makes ions drift faster in westward direction from nightside to dayside, where they begin to slow down due to increasing magnetic field, resulting in an accumulation of ion pressure in the post-dawn sector and depletion of ion pressure in the morning sector, and the symmetry of ring current is broken down.

Beyond the setup of time-dependent magnetic field, we established three different types of inductive electric field models (which are the MLT dependent electric field, propagating Gaussian pulse electric field, and the self-consistent inductive electric field), and tested their effects on the ring current ions. The MLT dependent electric field serves to accelerate the westward azimuthal drift of ions everywhere on the equatorial plane, expel ions away from the Earth in the postdawn sector, and injects ion inward in the morning and evening sectors, in correspondence to its dawn-dusk polarization direction. However, the superposition of such dawn-dusk electric field that is MLT dependent does not help ions overcome the dayside magnetic barrier, because it is symmetric around midnight — noon meridian. The propagating Gaussian pulse electric field is found to act as a transient but intensive local accelerator that can rapidly and effectively energize the particles from low energy to high energy in a short time interval and spatial distance, supporting the observations that ions with initial energy of tens of keV can be accelerated up to hundreds of keV on nightside during substorms. Moreover, the pulse electric field also triggers significant local radial Earthward transport of ions at the measurement point as it goes, regardless of the ions' energy, which can be the cause of observed nightside BBFs during substorms. However, this type of localized and transient inductive electric field model ignores the continuous changes in the geomagnetic field, and mis-estimates the changes in the drifts, energy, and pitch angles, as the local changes in the magnetic field set up a global inductive electric field.

Finally, we developed an algorithm to calculate the self-consistent equatorial inductive electric field associated with the time-changing magnetic field, by numerically performing the Biot-Savart like integration over a finite spherical domain, discretized by spherical grid cells that are static and not field-aligned. This field acts to radially trans-

port ions toward the Earth on nightside while expelling them away from the Earth on dayside during the stretching phase of magnetic field, and reverses in the dipolarization phase, therefore significantly altering the ion convection patterns. As a result, during the stretching phase, the self-consistent inductive electric field acts to further increase the ion pressure in the evening sector, and to decrease it in the morning sector. During the dipolarization phase, it tends to reverse the process in stretching phase. We showed that, the rapidly changing magnetic field produces large inductive electric field that can dominate over the electrostatic field. Consequently, not taking the effect of inductive electric field (even if changes of magnetic gradient-curvature drift have been considered) into account leads to a mis-estimation on the kinematics of ring current ion species and the associated ring current evolution over time.

A Geocentric Distance of Equatorial Intersections of Magnetic Field Lines with Different Footpoints, under Different Stretching Factors

In this appendix section, we attach the geocentric distance R_{eq} of equatorial intersections of the asymmetrically stretched magnetic field lines discussed in Section 2.2, under three different stretching factors $b = 0, 0.2, 0.4$ within three tables, respectively. In each table, λ_0 represents the magnetic latitude of the footpoint of certain magnetic field line, and ϕ_0 denotes the azimuthal angle of the equatorial intersection of certain field line. For each individual field line, R_{eq} is obtained by first solving the equation of field line (which is Equation 16) for L (providing $\lambda = \lambda_0$, stretching factor $\alpha = a + b \cdot cos\phi_0$ and $R = R_E$), then solving Equation 16 again (providing L that was just solved) for $R = R_{eq}$. The magnetic field configuration plot showed in Figure 1 can be generated with the data recorded in this section.

Table A.1. Dipole Magnetic Field ($a = 1$ and $b = 0$)

	$\lambda_0 = 60^\circ$	$\lambda_0 = 52^\circ$	$\lambda_0 = 45^\circ$	$\lambda_0 = 30^\circ$
$\phi_0 = 0$ (midnight)	$L = 4$ $R_{eq} = 4R_e$	$L = 2.638$ $R_{eq} = 2.638R_e$	$L = 2$ $R_{eq} = 2R_e$	$L = 1.333$ $R_{eq} = 1.333R_e$
$\phi_0 = \frac{\pi}{12}$	$L = 4$ $R_{eq} = 4R_e$	$L = 2.638$ $R_{eq} = 2.638R_e$	$L = 2$ $R_{eq} = 2R_e$	$L = 1.333$ $R_{eq} = 1.333R_e$
$\phi_0 = \frac{\pi}{6}$	$L = 4$ $R_{eq} = 4R_e$	$L = 2.638$ $R_{eq} = 2.638R_e$	$L = 2$ $R_{eq} = 2R_e$	$L = 1.333$ $R_{eq} = 1.333R_e$
$\phi_0 = \frac{\pi}{4}$	$L = 4$ $R_{eq} = 4R_e$	$L = 2.638$ $R_{eq} = 2.638R_e$	$L = 2$ $R_{eq} = 2R_e$	$L = 1.333$ $R_{eq} = 1.333R_e$
$\phi_0 = \frac{\pi}{3}$	$L = 4$ $R_{eq} = 4R_e$	$L = 2.638$ $R_{eq} = 2.638R_e$	$L = 2$ $R_{eq} = 2R_e$	$L = 1.333$ $R_{eq} = 1.333R_e$
$\phi_0 = \frac{5\pi}{12}$	$L = 4$ $R_{eq} = 4R_e$	$L = 2.638$ $R_{eq} = 2.638R_e$	$L = 2$ $R_{eq} = 2R_e$	$L = 1.333$ $R_{eq} = 1.333R_e$
$\phi_0 = \frac{\pi}{2}$ (dawn)	$L = 4$ $R_{eq} = 4R_e$	$L = 2.638$ $R_{eq} = 2.638R_e$	$L = 2$ $R_{eq} = 2R_e$	$L = 1.333$ $R_{eq} = 1.333R_e$
$\phi_0 = \frac{7\pi}{12}$	$L = 4$ $R_{eq} = 4R_e$	$L = 2.638$ $R_{eq} = 2.638R_e$	$L = 2$ $R_{eq} = 2R_e$	$L = 1.333$ $R_{eq} = 1.333R_e$
$\phi_0 = \frac{2\pi}{3}$	$L = 4$ $R_{eq} = 4R_e$	$L = 2.638$ $R_{eq} = 2.638R_e$	$L = 2$ $R_{eq} = 2R_e$	$L = 1.333$ $R_{eq} = 1.333R_e$
$\phi_0 = \frac{3\pi}{4}$	$L = 4$ $R_{eq} = 4R_e$	$L = 2.638$ $R_{eq} = 2.638R_e$	$L = 2$ $R_{eq} = 2R_e$	$L = 1.333$ $R_{eq} = 1.333R_e$
$\phi_0 = \frac{5\pi}{6}$	$L = 4$ $R_{eq} = 4R_e$	$L = 2.638$ $R_{eq} = 2.638R_e$	$L = 2$ $R_{eq} = 2R_e$	$L = 1.333$ $R_{eq} = 1.333R_e$
$\phi_0 = \frac{11\pi}{12}$	$L = 4$ $R_{eq} = 4R_e$	$L = 2.638$ $R_{eq} = 2.638R_e$	$L = 2$ $R_{eq} = 2R_e$	$L = 1.333$ $R_{eq} = 1.333R_e$
$\phi_0 = \pi$ (noon)	$L = 4$ $R_{eq} = 4R_e$	$L = 2.638$ $R_{eq} = 2.638R_e$	$L = 2$ $R_{eq} = 2R_e$	$L = 1.333$ $R_{eq} = 1.333R_e$
$\phi_0 = \frac{13\pi}{12}$	$L = 4$ $R_{eq} = 4R_e$	$L = 2.638$ $R_{eq} = 2.638R_e$	$L = 2$ $R_{eq} = 2R_e$	$L = 1.333$ $R_{eq} = 1.333R_e$
$\phi_0 = \frac{7\pi}{6}$	$L = 4$ $R_{eq} = 4R_e$	$L = 2.638$ $R_{eq} = 2.638R_e$	$L = 2$ $R_{eq} = 2R_e$	$L = 1.333$ $R_{eq} = 1.333R_e$
$\phi_0 = \frac{5\pi}{4}$	$L = 4$ $R_{eq} = 4R_e$	$L = 2.638$ $R_{eq} = 2.638R_e$	$L = 2$ $R_{eq} = 2R_e$	$L = 1.333$ $R_{eq} = 1.333R_e$
$\phi_0 = \frac{4\pi}{3}$	$L = 4$ $R_{eq} = 4R_e$	$L = 2.638$ $R_{eq} = 2.638R_e$	$L = 2$ $R_{eq} = 2R_e$	$L = 1.333$ $R_{eq} = 1.333R_e$
$\phi_0 = \frac{17\pi}{12}$	$L = 4$ $R_{eq} = 4R_e$	$L = 2.638$ $R_{eq} = 2.638R_e$	$L = 2$ $R_{eq} = 2R_e$	$L = 1.333$ $R_{eq} = 1.333R_e$
$\phi_0 = \frac{3\pi}{2}$ (dusk)	$L = 4$ $R_{eq} = 4R_e$	$L = 2.638$ $R_{eq} = 2.638R_e$	$L = 2$ $R_{eq} = 2R_e$	$L = 1.333$ $R_{eq} = 1.333R_e$
$\phi_0 = \frac{19\pi}{12}$	$L = 4$ $R_{eq} = 4R_e$	$L = 2.638$ $R_{eq} = 2.638R_e$	$L = 2$ $R_{eq} = 2R_e$	$L = 1.333$ $R_{eq} = 1.333R_e$
$\phi_0 = \frac{5\pi}{3}$	$L = 4$ $R_{eq} = 4R_e$	$L = 2.638$ $R_{eq} = 2.638R_e$	$L = 2$ $R_{eq} = 2R_e$	$L = 1.333$ $R_{eq} = 1.333R_e$
$\phi_0 = \frac{7\pi}{4}$	$L = 4$ $R_{eq} = 4R_e$	$L = 2.638$ $R_{eq} = 2.638R_e$	$L = 2$ $R_{eq} = 2R_e$	$L = 1.333$ $R_{eq} = 1.333R_e$
$\phi_0 = \frac{11\pi}{6}$	$L = 4$ $R_{eq} = 4R_e$	$L = 2.638$ $R_{eq} = 2.638R_e$	$L = 2$ $R_{eq} = 2R_e$	$L = 1.333$ $R_{eq} = 1.333R_e$
$\phi_0 = \frac{23\pi}{12}$	$L = 4$ $R_{eq} = 4R_e$	$L = 2.638$ $R_{eq} = 2.638R_e$	$L = 2$ $R_{eq} = 2R_e$	$L = 1.333$ $R_{eq} = 1.333R_e$

Table A.2. Under Stretching Factor $a = 1, b = 0.2$

	$\lambda_0 = 60^\circ$	$\lambda_0 = 52^\circ$	$\lambda_0 = 45^\circ$	$\lambda_0 = 30^\circ$
$\phi_0 = 0$ (midnight)	$L = 3.796$ $R_{eq} = 4.556R_e$	$L = 2.442$ $R_{eq} = 2.931R_e$	$L = 1.811$ $R_{eq} = 2.173R_e$	$L = 1.156$ $R_{eq} = 1.387R_e$
$\phi_0 = \frac{\pi}{12}$	$L = 3.816$ $R_{eq} = 4.507R_e$	$L = 2.460$ $R_{eq} = 2.906R_e$	$L = 1.828$ $R_{eq} = 2.159R_e$	$L = 1.171$ $R_{eq} = 1.383R_e$
$\phi_0 = \frac{\pi}{6}$	$L = 3.866$ $R_{eq} = 4.378R_e$	$L = 2.508$ $R_{eq} = 2.839R_e$	$L = 1.872$ $R_{eq} = 2.120R_e$	$L = 1.211$ $R_{eq} = 1.372R_e$
$\phi_0 = \frac{\pi}{4}$	$L = 3.926$ $R_{eq} = 4.213R_e$	$L = 2.566$ $R_{eq} = 2.753R_e$	$L = 1.928$ $R_{eq} = 2.069R_e$	$L = 1.264$ $R_{eq} = 1.356R_e$
$\phi_0 = \frac{\pi}{3}$	$L = 3.974$ $R_{eq} = 4.077R_e$	$L = 2.612$ $R_{eq} = 2.680R_e$	$L = 1.974$ $R_{eq} = 2.025R_e$	$L = 1.308$ $R_{eq} = 1.342R_e$
$\phi_0 = \frac{5\pi}{12}$	$L = 3.996$ $R_{eq} = 4.011R_e$	$L = 2.635$ $R_{eq} = 2.644R_e$	$L = 1.996$ $R_{eq} = 2.004R_e$	$L = 1.330$ $R_{eq} = 1.335R_e$
$\phi_0 = \frac{\pi}{2}$ (dawn)	$L = 4$ $R_{eq} = 4R_e$	$L = 2.638$ $R_{eq} = 2.638R_e$	$L = 2$ $R_{eq} = 2R_e$	$L = 1.333$ $R_{eq} = 1.333R_e$
$\phi_0 = \frac{7\pi}{12}$	$L = 4.003$ $R_{eq} = 3.990R_e$	$L = 2.642$ $R_{eq} = 2.633R_e$	$L = 2.003$ $R_{eq} = 1.997R_e$	$L = 1.337$ $R_{eq} = 1.332R_e$
$\phi_0 = \frac{2\pi}{3}$	$L = 4.024$ $R_{eq} = 3.927R_e$	$L = 2.662$ $R_{eq} = 2.598R_e$	$L = 2.024$ $R_{eq} = 1.976R_e$	$L = 1.358$ $R_{eq} = 1.325R_e$
$\phi_0 = \frac{3\pi}{4}$	$L = 4.067$ $R_{eq} = 3.791R_e$	$L = 2.707$ $R_{eq} = 2.522R_e$	$L = 2.069$ $R_{eq} = 1.928R_e$	$L = 1.404$ $R_{eq} = 1.309R_e$
$\phi_0 = \frac{5\pi}{6}$	$L = 4.124$ $R_{eq} = 3.602R_e$	$L = 2.766$ $R_{eq} = 2.415R_e$	$L = 2.130$ $R_{eq} = 1.861R_e$	$L = 1.471$ $R_{eq} = 1.284R_e$
$\phi_0 = \frac{11\pi}{12}$	$L = 4.174$ $R_{eq} = 3.427R_e$	$L = 2.818$ $R_{eq} = 2.314R_e$	$L = 2.186$ $R_{eq} = 1.795R_e$	$L = 1.534$ $R_{eq} = 1.259R_e$
$\phi_0 = \pi$ (noon)	$L = 4.193$ $R_{eq} = 3.355R_e$	$L = 2.839$ $R_{eq} = 2.271R_e$	$L = 2.209$ $R_{eq} = 1.767R_e$	$L = 1.561$ $R_{eq} = 1.248R_e$
$\phi_0 = \frac{13\pi}{12}$	$L = 4.174$ $R_{eq} = 3.427R_e$	$L = 2.818$ $R_{eq} = 2.314R_e$	$L = 2.186$ $R_{eq} = 1.795R_e$	$L = 1.534$ $R_{eq} = 1.259R_e$
$\phi_0 = \frac{7\pi}{6}$	$L = 4.124$ $R_{eq} = 3.602R_e$	$L = 2.766$ $R_{eq} = 2.415R_e$	$L = 2.130$ $R_{eq} = 1.861R_e$	$L = 1.471$ $R_{eq} = 1.284R_e$
$\phi_0 = \frac{5\pi}{4}$	$L = 4.067$ $R_{eq} = 3.791R_e$	$L = 2.707$ $R_{eq} = 2.522R_e$	$L = 2.069$ $R_{eq} = 1.928R_e$	$L = 1.404$ $R_{eq} = 1.309R_e$
$\phi_0 = \frac{4\pi}{3}$	$L = 4.024$ $R_{eq} = 3.927R_e$	$L = 2.662$ $R_{eq} = 2.598R_e$	$L = 2.024$ $R_{eq} = 1.976R_e$	$L = 1.358$ $R_{eq} = 1.325R_e$
$\phi_0 = \frac{17\pi}{12}$	$L = 4.003$ $R_{eq} = 3.990R_e$	$L = 2.642$ $R_{eq} = 2.633R_e$	$L = 2.003$ $R_{eq} = 1.997R_e$	$L = 1.337$ $R_{eq} = 1.332R_e$
$\phi_0 = \frac{3\pi}{2}$ (dusk)	$L = 4$ $R_{eq} = 4R_e$	$L = 2.638$ $R_{eq} = 2.638R_e$	$L = 2$ $R_{eq} = 2R_e$	$L = 1.333$ $R_{eq} = 1.333R_e$
$\phi_0 = \frac{19\pi}{12}$	$L = 3.996$ $R_{eq} = 4.011R_e$	$L = 2.635$ $R_{eq} = 2.644R_e$	$L = 1.996$ $R_{eq} = 2.004R_e$	$L = 1.330$ $R_{eq} = 1.335R_e$
$\phi_0 = \frac{5\pi}{3}$	$L = 3.974$ $R_{eq} = 4.077R_e$	$L = 2.612$ $R_{eq} = 2.680R_e$	$L = 1.974$ $R_{eq} = 2.025R_e$	$L = 1.308$ $R_{eq} = 1.342R_e$
$\phi_0 = \frac{7\pi}{4}$	$L = 3.926$ $R_{eq} = 4.213R_e$	$L = 2.566$ $R_{eq} = 2.753R_e$	$L = 1.928$ $R_{eq} = 2.069R_e$	$L = 1.264$ $R_{eq} = 1.356R_e$
$\phi_0 = \frac{11\pi}{6}$	$L = 3.866$ $R_{eq} = 4.378R_e$	$L = 2.508$ $R_{eq} = 2.839R_e$	$L = 1.872$ $R_{eq} = 2.120R_e$	$L = 1.211$ $R_{eq} = 1.372R_e$
$\phi_0 = \frac{23\pi}{12}$	$L = 3.816$ $R_{eq} = 4.507R_e$	$L = 2.460$ $R_{eq} = 2.906R_e$	$L = 1.828$ $R_{eq} = 2.159R_e$	$L = 1.171$ $R_{eq} = 1.383R_e$

Table A.3. Under Stretching Factor $a = 1, b = 0.4$

	$\lambda_0 = 60^\circ$	$\lambda_0 = 52^\circ$	$\lambda_0 = 45^\circ$	$\lambda_0 = 30^\circ$
$\phi_0 = 0$ (midnight)	$L = 3.592$ $R_{eq} = 5.030R_e$	$L = 2.259$ $R_{eq} = 3.163R_e$	$L = 1.644$ $R_{eq} = 2.302R_e$	$L = 1.017$ $R_{eq} = 1.423R_e$
$\phi_0 = \frac{\pi}{12}$	$L = 3.629$ $R_{eq} = 4.950R_e$	$L = 2.291$ $R_{eq} = 3.125R_e$	$L = 1.672$ $R_{eq} = 2.281R_e$	$L = 1.040$ $R_{eq} = 1.418R_e$
$\phi_0 = \frac{\pi}{6}$	$L = 3.726$ $R_{eq} = 4.727R_e$	$L = 2.378$ $R_{eq} = 3.017R_e$	$L = 1.751$ $R_{eq} = 2.221R_e$	$L = 1.105$ $R_{eq} = 1.401R_e$
$\phi_0 = \frac{\pi}{4}$	$L = 3.848$ $R_{eq} = 4.425R_e$	$L = 2.490$ $R_{eq} = 2.864R_e$	$L = 1.856$ $R_{eq} = 2.134R_e$	$L = 1.196$ $R_{eq} = 1.376R_e$
$\phi_0 = \frac{\pi}{3}$	$L = 3.946$ $R_{eq} = 4.157R_e$	$L = 2.585$ $R_{eq} = 2.723R_e$	$L = 1.947$ $R_{eq} = 2.051R_e$	$L = 1.282$ $R_{eq} = 1.350R_e$
$\phi_0 = \frac{5\pi}{12}$	$L = 3.993$ $R_{eq} = 4.022R_e$	$L = 2.631$ $R_{eq} = 2.650R_e$	$L = 1.993$ $R_{eq} = 2.007R_e$	$L = 1.326$ $R_{eq} = 1.336R_e$
$\phi_0 = \frac{\pi}{2}$ (dawn)	$L = 4$ $R_{eq} = 4R_e$	$L = 2.638$ $R_{eq} = 2.638R_e$	$L = 2$ $R_{eq} = 2R_e$	$L = 1.333$ $R_{eq} = 1.333R_e$
$\phi_0 = \frac{7\pi}{12}$	$L = 4.007$ $R_{eq} = 3.980R_e$	$L = 2.645$ $R_{eq} = 2.627R_e$	$L = 2.007$ $R_{eq} = 1.993R_e$	$L = 1.340$ $R_{eq} = 1.331R_e$
$\phi_0 = \frac{2\pi}{3}$	$L = 4.046$ $R_{eq} = 3.859R_e$	$L = 2.684$ $R_{eq} = 2.561R_e$	$L = 2.047$ $R_{eq} = 1.952R_e$	$L = 1.381$ $R_{eq} = 1.317R_e$
$\phi_0 = \frac{3\pi}{4}$	$L = 4.127$ $R_{eq} = 3.591R_e$	$L = 2.769$ $R_{eq} = 2.409R_e$	$L = 2.134$ $R_{eq} = 1.857R_e$	$L = 1.474$ $R_{eq} = 1.283R_e$
$\phi_0 = \frac{5\pi}{6}$	$L = 4.234$ $R_{eq} = 3.198R_e$	$L = 2.883$ $R_{eq} = 2.178R_e$	$L = 2.257$ $R_{eq} = 1.705R_e$	$L = 1.620$ $R_{eq} = 1.223R_e$
$\phi_0 = \frac{11\pi}{12}$	$L = 4.327$ $R_{eq} = 2.799R_e$	$L = 2.988$ $R_{eq} = 1.933R_e$	$L = 2.375$ $R_{eq} = 1.536R_e$	$L = 1.776$ $R_{eq} = 1.149R_e$
$\phi_0 = \pi$ (noon)	$L = 4.364$ $R_{eq} = 2.619R_e$	$L = 3.031$ $R_{eq} = 1.819R_e$	$L = 2.425$ $R_{eq} = 1.455R_e$	$L = 1.849$ $R_{eq} = 1.109R_e$
$\phi_0 = \frac{13\pi}{12}$	$L = 4.327$ $R_{eq} = 2.799R_e$	$L = 2.988$ $R_{eq} = 1.933R_e$	$L = 2.375$ $R_{eq} = 1.536R_e$	$L = 1.776$ $R_{eq} = 1.149R_e$
$\phi_0 = \frac{7\pi}{6}$	$L = 4.234$ $R_{eq} = 3.198R_e$	$L = 2.883$ $R_{eq} = 2.178R_e$	$L = 2.257$ $R_{eq} = 1.705R_e$	$L = 1.620$ $R_{eq} = 1.223R_e$
$\phi_0 = \frac{5\pi}{4}$	$L = 4.127$ $R_{eq} = 3.591R_e$	$L = 2.769$ $R_{eq} = 2.409R_e$	$L = 2.134$ $R_{eq} = 1.857R_e$	$L = 1.474$ $R_{eq} = 1.283R_e$
$\phi_0 = \frac{4\pi}{3}$	$L = 4.046$ $R_{eq} = 3.859R_e$	$L = 2.684$ $R_{eq} = 2.561R_e$	$L = 2.047$ $R_{eq} = 1.952R_e$	$L = 1.381$ $R_{eq} = 1.317R_e$
$\phi_0 = \frac{17\pi}{12}$	$L = 4.007$ $R_{eq} = 3.980R_e$	$L = 2.645$ $R_{eq} = 2.627R_e$	$L = 2.007$ $R_{eq} = 1.993R_e$	$L = 1.340$ $R_{eq} = 1.331R_e$
$\phi_0 = \frac{3\pi}{2}$ (dusk)	$L = 4$ $R_{eq} = 4R_e$	$L = 2.638$ $R_{eq} = 2.638R_e$	$L = 2$ $R_{eq} = 2R_e$	$L = 1.333$ $R_{eq} = 1.333R_e$
$\phi_0 = \frac{19\pi}{12}$	$L = 3.993$ $R_{eq} = 4.022R_e$	$L = 2.631$ $R_{eq} = 2.650R_e$	$L = 1.993$ $R_{eq} = 2.007R_e$	$L = 1.326$ $R_{eq} = 1.336R_e$
$\phi_0 = \frac{5\pi}{3}$	$L = 3.946$ $R_{eq} = 4.157R_e$	$L = 2.585$ $R_{eq} = 2.723R_e$	$L = 1.947$ $R_{eq} = 2.051R_e$	$L = 1.282$ $R_{eq} = 1.350R_e$
$\phi_0 = \frac{7\pi}{4}$	$L = 3.848$ $R_{eq} = 4.425R_e$	$L = 2.490$ $R_{eq} = 2.864R_e$	$L = 1.856$ $R_{eq} = 2.134R_e$	$L = 1.196$ $R_{eq} = 1.376R_e$
$\phi_0 = \frac{11\pi}{6}$	$L = 3.726$ $R_{eq} = 4.727R_e$	$L = 2.378$ $R_{eq} = 3.017R_e$	$L = 1.751$ $R_{eq} = 2.221R_e$	$L = 1.105$ $R_{eq} = 1.401R_e$
$\phi_0 = \frac{23\pi}{12}$	$L = 3.629$ $R_{eq} = 4.950R_e$	$L = 2.291$ $R_{eq} = 3.125R_e$	$L = 1.672$ $R_{eq} = 2.281R_e$	$L = 1.040$ $R_{eq} = 1.418R_e$

Acknowledgments

Work at University of Illinois at Urbana-Champaign was performed with financial support from the NASA grant 3004631577, the NSF ICER 16-64078, NSF AGS 14-30292, NSF AGS 16-02734, and the NSF CAREER Award AGS 19-45573. The HEIDI model has been included in the Space Weather Modeling Framework, which is available for download at http://csem.engin.umich.edu/tools/swmf/. The full set of simulation data is available at https://doi.org/10.6084/m9.figshare.c.5083280.v1.

References

Angelopoulos, V., Kennel, C. F., Coroniti, F. V., Pellat, R., Kivelson, M. G., Walker, R. J., ... Gosling, J. T. (1994, November). Statistical characteristics of bursty bulk flow events. *Journal of Geophysical Research (ISSN 0148-0227)*, *99*, 21257.

Angelopoulos, V., Runov, A., Zhou, X., Turner, D. L., Kiehas, S. A., Li, S., & Shinohara, I. (2013, December). Electromagnetic energy conversion at reconnection fronts. In *Agu fall meeting abstracts* (Vol. 2013, p. SM13E-04).

Angelopoulos, V., Temerin, M., Roth, I., Mozer, F. S., Weimer, D., & Hairston, M. R. (2002). Testing global storm-time electric field models using particle spectra on multiple spacecraft. *Journal of Geophysical Research: Space Physics*, *107*(A8), SMP 21-1-SMP 21-11. Retrieved from `https://agupubs.onlinelibrary.wiley.com/doi/abs/10.1029/2001JA900174` doi: 10.1029/2001JA900174

Antonova, E., & Ganushkina, N. (1997). Azimuthal hot plasma pressure gradients and dawn-dusk electric field formation. *Journal of Atmospheric and Solar-Terrestrial Physics*, *59*(11), 1343 - 1354. Retrieved from `http://www.sciencedirect.com/science/article/pii/S1364682696001691` doi: http://dx.doi.org/10.1016/S1364-6826(96)00169-1

Artemyev, A. V., Liu, J., Angelopoulos, V., & Runov, A. (2015). Acceleration of ions by electric field pulses in the inner magnetosphere. *Journal of Geophysical Research: Space Physics*, *120*(6), 4628-4640. Retrieved from `https://agupubs.onlinelibrary.wiley.com/doi/abs/10.1002/2015JA021160` doi: 10.1002/2015JA021160

Ashour-Abdalla, M., Bosqued, J.-M., El-Alaoui, M., Peroomian, V., Zhou, M.,

Richard, R., ... Angelopoulos, V. (2009). A simulation study of particle energization observed by themis spacecraft during a substorm. *Journal of Geophysical Research: Space Physics*, *114*(A9). Retrieved from https://agupubs.onlinelibrary.wiley.com/doi/abs/10.1029/2009JA014126 doi: 10.1029/2009JA014126

Belian, R. D., Baker, D. N., Higbie, P. R., & Hones Jr., E. W. (1978, October). High-resolution energetic particle measurements at 6.6 re, 2. high-energy proton drift echoes. *Journal of Geophysical Research: Space Physics*, *83*(A10), 4857-4862. Retrieved from https://agupubs.onlinelibrary.wiley.com/doi/abs/10.1029/JA083iA10p04857 doi: 10.1029/JA083iA10p04857

Birn, J., Thomsen, M. F., Borovsky, J. E., Reeves, G. D., McComas, D. J., & Belian, R. D. (1997, February). Characteristic plasma properties during dispersionless substorm injections at geosynchronous orbit. *Journal of Geophysical Research: Space Physics (1978–2012)*, *102*(A2), 2309–2324.

Birn, J., Thomsen, M. F., Borovsky, J. E., Reeves, G. D., McComas, D. J., Belian, R. D., & Hesse, M. (1997, February). Substorm ion injections: Geosynchronous observations and test particle orbits in three-dimensional dynamic MHD fields. *Journal of Geophysical Research: Space Physics (1978–2012)*, *102*(A2), 2325–2341.

Birn, J., Thomsen, M. F., Borovsky, J. E., Reeves, G. D., McComas, D. J., Belian, R. D., & Hesse, M. (1998). Substorm electron injections: Geosynchronous observations and test particle simulations. *Journal of Geophysical Research: Space Physics*, *103*(A5), 9235-9248. Retrieved from https://agupubs.onlinelibrary.wiley.com/doi/abs/10.1029/97JA02635 doi: 10.1029/97JA02635

Califf, S., Li, X., Blum, L., Jaynes, A., Schiller, Q., Zhao, H., ... Bonnell, J. W. (2014). Themis measurements of quasi-static electric fields in the inner magnetosphere. *Journal of Geophysical Research: Space Physics*, *119*(12), 9939-9951. Retrieved from https://agupubs.onlinelibrary.wiley.com/doi/abs/10.1002/2014JA020360 doi: 10.1002/2014JA020360

Delcourt, D. C. (2002). Particle acceleration by inductive electric fields in the inner magnetosphere. *Journal of Atmospheric and Solar-Terrestrial Physics*.

Ebihara, Y., & Ejiri, M. (1998, October). Modeling of solar wind control of the

ring current buildup: A case study of the magnetic storms in April 1997. , *25*, 3751-3754. doi: 10.1029/1998GL900006

Fok, M., & Moore, T. E. (1997, July). Ring current modeling in a realistic magnetic field configuration. , *24*, 1775-1778. doi: 10.1029/97GL01255

Fok, M. C., Moore, T. E., & Greenspan, M. E. (1996, July). Ring current development during storm main phase. *Journal of Geophysical Research: Space Physics*, *101*(A7), 15311–15322.

Gabrielse, C., Angelopoulos, V., Runov, A., & Turner, D. L. (2012). The effects of transient, localized electric fields on equatorial electron acceleration and transport toward the inner magnetosphere. *Journal of Geophysical Research: Space Physics*, *117*(A10). Retrieved from `https://agupubs.onlinelibrary.wiley.com/doi/abs/10.1029/2012JA017873` doi: 10.1029/2012JA017873

Gabrielse, C., Angelopoulos, V., Runov, A., & Turner, D. L. (2014). Statistical characteristics of particle injections throughout the equatorial magnetotail. *Journal of Geophysical Research: Space Physics*, *119*(4), 2512-2535. Retrieved from `https://agupubs.onlinelibrary.wiley.com/doi/abs/10.1002/2013JA019638` doi: 10.1002/2013JA019638

Gabrielse, C., Harris, C., Angelopoulos, V., Artemyev, A., & Runov, A. (2016). The role of localized inductive electric fields in electron injections around dipolarizing flux bundles. *Journal of Geophysical Research: Space Physics*, *121*(10), 9560-9585. Retrieved from `https://agupubs.onlinelibrary.wiley.com/doi/abs/10.1002/2016JA023061` doi: 10.1002/2016JA023061

Ganushkina, N. Y., Amariutei, O. A., Shprits, Y. Y., & Liemohn, M. W. (2013, January). Transport of the plasma sheet electrons to the geostationary distances. *Journal of Geophysical Research: Space Physics*, *118*(1), 82–98.

Ganushkina, N. Y., Liemohn, M. W., & Pulkkinen, T. I. (2012, January). Storm-time ring current: model-dependent results. *Annales Geophysicae*, *30*, 177-202. doi: 10.5194/angeo-30-177-2012

Ganushkina, N. Y., Pulkkinen, T. I., Bashkirov, V. F., Baker, D. N., & Li, X. (2001, February). Formation of intense nose structures. , *28*, 491-494. doi: 10.1029/2000GL011955

Ganushkina, N. Y., Pulkkinen, T. I., & Fritz, T. (2005, February). Role of substorm-

associated impulsive electric fields in the ring current development during storms. *Annales Geophysicae*, *23*, 579-591. doi: 10.5194/angeo-23-579-2005

Holter, ., Altman, C., Roux, A., Perraut, S., Pedersen, A., Pcseli, H., ... Kremser, G. (1995). Characterization of low frequency oscillations at substorm breakup. *Journal of Geophysical Research: Space Physics*, *100*(A10), 19109-19119. Retrieved from `https://agupubs.onlinelibrary.wiley.com/doi/abs/10.1029/95JA00990` doi: 10.1029/95JA00990

Ilie, R., Daldorff, L. K. S., Liemohn, M. W., Toth, G., & Chan, A. A. (2017, May). Calculating the inductive electric field in the terrestrial magnetosphere. *Journal of Geophysical Research: Space Physics*, *122*(5), 5391–5403.

Ilie, R., Liemohn, M. W., Toth, G., & Skoug, R. M. (2012). Kinetic model of the inner magnetosphere with arbitrary magnetic field. *Journal of Geophysical Research: Space Physics*, *117*(A4). doi: 10.1029/2011JA017189

Ingraham, J. C., Cayton, T. E., Belian, R. D., Christensen, R. A., Friedel, R. H. W., Meier, M. M., ... Tuszewski, M. (2001). Substorm injection of relativistic electrons to geosynchronous orbit during the great magnetic storm of march 24, 1991. *Journal of Geophysical Research: Space Physics*, *106*(A11), 25759-25776. Retrieved from `https://agupubs.onlinelibrary.wiley.com/doi/abs/10.1029/2000JA000458` doi: 10.1029/2000JA000458

Kivelson, M. G., & Russell, C. T. (1995). *Introduction to Space Physics*. Cambridge University Press.

Lejosne, S., & Mozer, F. S. (2016). Typical values of the electric drift eb/b2 in the inner radiation belt and slot region as determined from van allen probe measurements. *Journal of Geophysical Research: Space Physics*, *121*(12), 12,014-12,024. Retrieved from `https://agupubs.onlinelibrary.wiley.com/doi/abs/10.1002/2016JA023613` doi: 10.1002/2016JA023613

Li, X., Baker, D. N., Temerin, M., Reeves, G. D., & Belian, R. D. (1998). Simulation of dispersionless injections and drift echoes of energetic electrons associated with substorms. , *25*, 3763-3766. doi: 10.1029/1998GL900001

Li, X., Roth, I., Temerin, M., Wygant, J. R., Hudson, M. K., & Blake, J. B. (1993, November). Simulation of the prompt energization and transport of radiation belt particles during the March 24, 1991 SSC. *Geophysical Research Letters*, *20*(22), 2423–2426.

Li, X., Sarris, T. E., Baker, D. N., Peterson, W. K., & Singer, H. J. (2003). Simulation of energetic particle injections associated with a substorm on august 27, 2001. *Geophysical Research Letters*, *30*(1), 4-1-4-4. Retrieved from https://agupubs.onlinelibrary.wiley.com/doi/abs/10.1029/2002GL015967 doi: 10.1029/2002GL015967

Liemohn, M. W., Ridley, A. J., Gallagher, D. L., Ober, D. M., & Kozyra, J. U. (2004, March). Dependence of plasmaspheric morphology on the electric field description during the recovery phase of the 17 April 2002 magnetic storm. *Journal of Geophysical Research (Space Physics)*, *109*(A18), 3209-+. doi: 10.1029/2003JA010304

Liemohn, M. W., Ridley, A. J., Kozyra, J. U., Gallagher, D. L., Thomsen, M. F., Henderson, M. G., ... Goldstein, J. (2006, November). Analyzing electric field morphology through data-model comparisons of the Geospace Environment Modeling Inner Magnetosphere/Storm Assessment Challenge events. *Journal of Geophysical Research (Space Physics)*, *111*(A10), 11-+. doi: 10.1029/2006JA011700

Liu, J., Angelopoulos, V., Zhou, X.-Z., & Runov, A. (2014). Magnetic flux transport by dipolarizing flux bundles. *Journal of Geophysical Research: Space Physics*, *119*(2), 909-926. Retrieved from https://agupubs.onlinelibrary.wiley.com/doi/abs/10.1002/2013JA019395 doi: 10.1002/2013JA019395

Liu, W. L., Li, X., Sarris, T., Cully, C., Ergun, R., Angelopoulos, V., ... Auster, H. U. (2009). Observation and modeling of the injection observed by themis and lanl satellites during the 23 march 2007 substorm event. *Journal of Geophysical Research: Space Physics*, *114*(A1). Retrieved from https://agupubs.onlinelibrary.wiley.com/doi/abs/10.1029/2008JA013498 doi: 10.1029/2008JA013498

Lopez, R. E., Sibeck, D. G., McEntire, R. W., & Krimigis, S. M. (1990). The energetic ion substorm injection boundary. *Journal of Geophysical Research: Space Physics*, *95*(A1), 109-117. Retrieved from https://agupubs.onlinelibrary.wiley.com/doi/abs/10.1029/JA095iA01p00109 doi: 10.1029/JA095iA01p00109

Matsui, H., Jordanova, V. K., Quinn, J. M., Torbert, R. B., & Paschmann, G. (2004). Derivation of electric potential patterns in the inner magnetosphere

from cluster edi data: Initial results. *Journal of Geophysical Research: Space Physics*, *109*(A10). Retrieved from https://agupubs.onlinelibrary.wiley.com/doi/abs/10.1029/2003JA010319 doi: 10.1029/2003JA010319

Matsui, H., Quinn, J. M., Torbert, R. B., Jordanova, V. K., Baumjohann, W., Puhl-Quinn, P. A., & Paschmann, G. (2003). Electric field measurements in the inner magnetosphere by cluster edi. *Journal of Geophysical Research: Space Physics*, *108*(A9). Retrieved from https://agupubs.onlinelibrary.wiley.com/doi/abs/10.1029/2003JA009913 doi: 10.1029/2003JA009913

Mithaiwala, M. J., & Horton, W. (2005). Substorm injections produce sufficient electron energization to account for mev flux enhancements following some storms. *Journal of Geophysical Research: Space Physics*, *110*(A7). Retrieved from https://agupubs.onlinelibrary.wiley.com/doi/abs/10.1029/2004JA010511 doi: 10.1029/2004JA010511

Moore, T. E., Arnoldy, R. L., Feynman, J., & Hardy, D. A. (1981). Propagating substorm injection fronts. *Journal of Geophysical Research: Space Physics*, *86*(A8), 6713-6726. Retrieved from https://agupubs.onlinelibrary.wiley.com/doi/abs/10.1029/JA086iA08p06713 doi: 10.1029/JA086iA08p06713

Nakamura, R., Baumjohann, W., Klecker, B., Bogdanova, Y., Balogh, A., RéMe, H., ... Runov, A. (2002, October). Motion of the dipolarization front during a flow burst event observed by Cluster. *Geophysical Research Letters*, *29*(2), 1942.

Nakamura, R., Baumjohann, W., Panov, E., Volwerk, M., Birn, J., Artemyev, A., ... Khotyaintsev, Y. (2013). Flow bouncing and electron injection observed by cluster. *Journal of Geophysical Research: Space Physics*, *118*(5), 2055-2072. Retrieved from https://agupubs.onlinelibrary.wiley.com/doi/abs/10.1002/jgra.50134 doi: 10.1002/jgra.50134

Nishimura, Y., Kikuchi, T., Wygant, J., Shinbori, A., Ono, T., Matsuoka, A., ... Brautigam, D. (2009). Response of convection electric fields in the magnetosphere to imf orientation change. *Journal of Geophysical Research: Space Physics*, *114*(A9). Retrieved from https://agupubs.onlinelibrary.wiley.com/doi/abs/10.1029/2009JA014277 doi: 10.1029/2009JA014277

Nishimura, Y., Shinbori, A., Ono, T., Iizima, M., & Kumamoto, A. (2006). Storm-time electric field distribution in the inner magnetosphere. *Geophysical Re-*

search Letters, *33*(22). Retrieved from https://agupubs.onlinelibrary.wiley.com/doi/abs/10.1029/2006GL027510 doi: 10.1029/2006GL027510

Nishimura, Y., Shinbori, A., Ono, T., Iizima, M., & Kumamoto, A. (2007). Evolution of ring current and radiation belt particles under the influence of storm-time electric fields. *Journal of Geophysical Research: Space Physics*, *112*(A6). Retrieved from https://agupubs.onlinelibrary.wiley.com/doi/abs/10.1029/2006JA012177 doi: 10.1029/2006JA012177

Pedersen, A., Cattell, C. A., Flthammar, C.-G., Knott, K., Lindqvist, P.-A., Manka, R. H., & Mozer, F. S. (1985). Electric fields in the plasma sheet and plasma sheet boundary layer. *Journal of Geophysical Research: Space Physics*, *90*(A2), 1231-1242. Retrieved from https://agupubs.onlinelibrary.wiley.com/doi/abs/10.1029/JA090iA02p01231 doi: 10.1029/JA090iA02p01231

Richmond, A. D., Blanc, M., Emery, B. A., Wand, R. H., Fejer, B. G., Woodman, R. F., ... Evans, J. V. (1980). An empirical model of quiet-day ionospheric electric fields at middle and low latitudes. *Journal of Geophysical Research: Space Physics*, *85*(A9), 4658-4664. Retrieved from https://agupubs.onlinelibrary.wiley.com/doi/abs/10.1029/JA085iA09p04658 doi: 10.1029/JA085iA09p04658

Ridley, A. J., & Liemohn, M. W. (2002, August). A model-derived storm time asymmetric ring current driven electric field description. *Journal of Geophysical Research (Space Physics)*, *107*, 1151-+. doi: 10.1029/2001JA000051

Roederer, J. G. (1970). *Dynamics of geomagnetically trapped radiation.* New York: Springer-Verlag.

Rowland, D. E., & Wygant, J. R. (1998, July). Dependence of the large-scale, inner magnetospheric electric field on geomagnetic activity. , *103*, 14959-14964. doi: 10.1029/97JA03524

Runov, A., Angelopoulos, V., Gabrielse, C., Zhou, X.-Z., Turner, D., & Plaschke, F. (2013). Electron fluxes and pitch-angle distributions at dipolarization fronts: Themis multipoint observations. *Journal of Geophysical Research: Space Physics*, *118*(2), 744-755. Retrieved from https://agupubs.onlinelibrary.wiley.com/doi/abs/10.1002/jgra.50121 doi: 10.1002/jgra.50121

Runov, A., Angelopoulos, V., Sitnov, M. I., Sergeev, V. A., Bonnell, J., McFad-

den, J. P., ... Auster, U. (2009). Themis observations of an earthward-propagating dipolarization front. *Geophysical Research Letters*, *36*(14). Retrieved from https://agupubs.onlinelibrary.wiley.com/doi/abs/10.1029/2009GL038980 doi: 10.1029/2009GL038980

Runov, A., Angelopoulos, V., Zhou, X.-Z., Zhang, X.-J., Li, S., Plaschke, F., & Bonnell, J. (2011). A themis multicase study of dipolarization fronts in the magnetotail plasma sheet. *Journal of Geophysical Research: Space Physics*, *116*(A5). Retrieved from https://agupubs.onlinelibrary.wiley.com/doi/abs/10.1029/2010JA016316 doi: 10.1029/2010JA016316

Russell, C. T., & McPherron, R. L. (1973, November). The Magnetotail and Substorms. *Space Science Reviews*, *15*, 205-266. doi: 10.1007/BF00169321

Sarris, T. E., Li, X., Tsaggas, N., & Paschalidis, N. (2002, March). Modeling energetic particle injections in dynamic pulse fields with varying propagation speeds. *Journal of Geophysical Research (Space Physics)*, *107*, 1033. doi: 10.1029/2001JA900166

Sergeev, V., Angelopoulos, V., Apatenkov, S., Bonnell, J., Ergun, R., Nakamura, R., ... Runov, A. (2009a). Kinetic structure of the sharp injection/dipolarization front in the flow-braking region. *Geophysical Research Letters*, *36*(21). Retrieved from https://agupubs.onlinelibrary.wiley.com/doi/abs/10.1029/2009GL040658 doi: 10.1029/2009GL040658

Sergeev, V., Angelopoulos, V., Apatenkov, S., Bonnell, J., Ergun, R., Nakamura, R., ... Runov, A. (2009b). Kinetic structure of the sharp injection/dipolarization front in the flow-braking region. *Geophysical Research Letters*, *36*(21). Retrieved from https://agupubs.onlinelibrary.wiley.com/doi/abs/10.1029/2009GL040658 doi: 10.1029/2009GL040658

Sergeev, V. A., Angelopoulos, V., & Nakamura, R. (2012). Recent advances in understanding substorm dynamics. *Geophysical Research Letters*, *39*(5). Retrieved from https://agupubs.onlinelibrary.wiley.com/doi/abs/10.1029/2012GL050859 doi: 10.1029/2012GL050859

Sergeev, V. A., Chernyaev, I. A., Dubyagin, S. V., Miyashita, Y., Angelopoulos, V., Boakes, P. D., ... Henderson, M. G. (2012). Energetic particle injections to geostationary orbit: Relationship to flow bursts and magnetospheric state. *Journal of Geophysical Research: Space Physics*, *117*(A10). Retrieved

from https://agupubs.onlinelibrary.wiley.com/doi/abs/10.1029/2012JA017773 doi: 10.1029/2012JA017773

Sergeev, V. A., Shukhtina, M. A., Rasinkangas, R., Korth, A., Reeves, G. D., Singer, H. J., ... Vagina, L. I. (1998). Event study of deep energetic particle injections during substorm. *Journal of Geophysical Research: Space Physics*, *103*(A5), 9217-9234. Retrieved from https://agupubs.onlinelibrary.wiley.com/doi/abs/10.1029/97JA03686 doi: 10.1029/97JA03686

Spanswick, E., Donovan, E., Friedel, R., & Korth, A. (2007). Ground based identification of dispersionless electron injections. *Geophysical Research Letters*, *34*(3). Retrieved from https://agupubs.onlinelibrary.wiley.com/doi/abs/10.1029/2006GL028329 doi: 10.1029/2006GL028329

Spanswick, E., Reeves, G. D., Donovan, E., & Friedel, R. H. W. (2010). Injection region propagation outside of geosynchronous orbit. *Journal of Geophysical Research: Space Physics*, *115*(A11). Retrieved from https://agupubs.onlinelibrary.wiley.com/doi/abs/10.1029/2009JA015066 doi: 10.1029/2009JA015066

Stern, D. P. (1975). The motion of a proton in the equatorial magnetosphere. *J. Geophys. Res.*, *80*, 595.

Thaller, S. A., Wygant, J. R., Dai, L., Breneman, A. W., Kersten, K., Cattell, C. A., ... Bounds, S. R. (2015). Van allen probes investigation of the large-scale duskward electric field and its role in ring current formation and plasmasphere erosion in the 1 june 2013 storm. *Journal of Geophysical Research: Space Physics*, *120*(6), 4531-4543. Retrieved from https://agupubs.onlinelibrary.wiley.com/doi/abs/10.1002/2014JA020875 doi: 10.1002/2014JA020875

Thomsen, M. F., Birn, J., Borovsky, J. E., Morzinski, K., McComas, D. J., & Reeves, G. D. (2001). Two-satellite observations of substorm injections at geosynchronous orbit. *Journal of Geophysical Research: Space Physics*, *106*(A5), 8405-8416. Retrieved from https://agupubs.onlinelibrary.wiley.com/doi/abs/10.1029/2000JA000080 doi: 10.1029/2000JA000080

Toivanen, P. K. (2007). Deformation method for electromagnetic magnetospheric fields: 1. Theory. *Journal of Geophysical Research: Space Physics*, *112*(A6).

Volland, H. (1973). A semiempirical model of large-scale magnetospheric electric

fields. *J. Geophys. Res.*, *78*, 171.

Weimer, D. R. (1996). A flexible, IMF dependent model of high-latitude electric potentials having "space weather" applications. , *23*, 2549-2552. doi: 10.1029/96GL02255

Wygant, J., Rowland, D., Singer, H. J., Temerin, M., Mozer, F., & Hudson, M. K. (1998, December). Experimental evidence on the role of the large spatial scale electric field in creating the ring current. , *103*, 29527-29544. doi: 10.1029/98JA01436

Zaharia, S., Cheng, C. Z., & Johnson, J. R. (2000). Particle transport and energization associated with substorms. *Journal of Geophysical Research: Space Physics*, *105*(A8), 18741-18752. Retrieved from `https://agupubs.onlinelibrary.wiley.com/doi/abs/10.1029/1999JA000407` doi: 10.1029/1999JA000407

Zaharia, S., Jordanova, V. K., Thomsen, M. F., & Reeves, G. D. (2008, February). Self-consistent geomagnetic storm simulation: The role of the induced electric fields. *Journal of Atmospheric and Solar-Terrestrial Physics*, *70*.

Zaharia, S., Thomsen, M. F., Birn, J., Denton, M. H., Jordanova, V. K., & Cheng, C. Z. (2005, February). Effect of storm-time plasma pressure on the magnetic field in the inner magnetosphere. *Geophysical Research Letters*, *32*(3), 3102.

Zhao, H., Baker, D. N., Califf, S., Li, X., Jaynes, A. N., Leonard, T., ... Spence, H. E. (2017). Van allen probes measurements of energetic particle deep penetration into the low l region (l¡4) during the storm on 8 april 2016. *Journal of Geophysical Research: Space Physics*, *122*(12), 12,140-12,152. Retrieved from `https://agupubs.onlinelibrary.wiley.com/doi/abs/10.1002/2017JA024558` doi: 10.1002/2017JA024558